

Collective behavior of self-steering active particles with velocity alignment and visual perception

Rajendra Singh Negi^{*,} Roland G. Winkler^{†,} and Gerhard Gompper[‡]*Theoretical Physics of Living Matter, Institute of Biological Information Processing and Institute for Advanced Simulation, Forschungszentrum Jülich, 52428 Jülich, Germany*

(Received 11 July 2023; accepted 4 December 2023; published 29 January 2024)

The formation and dynamics of swarms is widespread in living systems, from bacterial biofilms to schools of fish and flocks of birds. We study this emergent collective behavior via agent-based simulations in a model of active Brownian particles with visual-perception-based steering and alignment interactions. The dynamics, shape, and internal structure of the emergent aggregates, clusters, and swarms of these intelligent active Brownian particles are determined by the maneuverabilities Ω_v and Ω_a , quantifying the steering based on the visual signal and polar alignment, respectively, the propulsion velocity, characterized by the Péclet number Pe , the vision angle θ , and the orientational noise. Various nonequilibrium dynamical aggregates—like motile wormlike swarms and milling, and close-packed or dispersed clusters—are obtained. Small vision angles imply the formation of small clusters, while large vision angles lead to more complex clusters. In particular, a strong polar-alignment maneuverability Ω_a favors elongated wormlike swarms, which display superdiffusive motion over a much longer time range than individual ABPs, whereas a strong vision-based maneuverability Ω_v favors compact, nearly immobile aggregates. Swarm trajectories show long persistent directed motion, interrupted by sharp turns. Milling rings, where a wormlike swarm bites its own tail, emerge for an intermediate regime of Pe and vision angles. Our results offer insights into the behavior of animal swarms and provide design criteria for swarming microbots.

DOI: [10.1103/PhysRevResearch.6.013118](https://doi.org/10.1103/PhysRevResearch.6.013118)

I. INTRODUCTION

Self-organized group formation and collective motion in the form of swarms or flocks is a hallmark of living systems over a wide range of length scales, from bacterial biofilms to schools of fish, flocks of birds, and animal herds [1–6]. This behavior emerges without central control and is rather governed by the response of individuals to the action of other group members or agents. The self-organized structures and motion typically extend over much larger length scales than the size of the individual units, and emergent properties and function achieved are beyond the capacity of constituent units [7–11]. Arising patterns and structures not only depend on the physical interactions between the various agents of an ensemble, but are often governed by nonreciprocal information input, e.g., visual perception in case of animals, processing of this information, and active response. Unravelling the underlying mechanisms and principles not only sheds light onto the behavior of biological systems but provides concepts to design functional synthetic active [2,12] and microrobotic [13]

systems, which are able to adopt to environmental conditions and perform complex tasks autonomously [14,15].

Several interactions and information-exchange processes can contribute to the formation of swarms and flocks. Correspondingly, various models have been proposed and analyzed to understand this process and the resulting structures.

A pertinent feature of the collective motion of animal groups is motion alignment and cohesion. In a pioneering work, Reynolds proposed three interaction rules for birdlike objects called boids, which are collision avoidance, velocity matching, and flock centering [16]. The boid model shares features with earlier models on fish schools which considered alignment with nearby individuals, attraction to the center of the school, and avoidance of close neighbors to prevent collisions [8,10]. A similar model is the behavioural zonal model by Couzin *et al.* [17,18], which considers different types of interactions between individuals in three nonoverlapping zones: repulsion, alignment with neighbors, and attraction toward other individuals, respectively. The analysis of this model shows complex structures like swarms, milling, and groups with highly parallel motion. From the physics perspective, perhaps the most celebrated model of collective motion is the Vicsek model [19] and its refinements and extensions [5,20–26]. In the basic version of this model, particles move with constant speed and change their direction at each time step by aligning with the mean orientation of neighboring particles in a prescribed interaction range, together with some noise accounting for environmental perturbations. The Vicsek model shows a phase transition from a disordered phase to an ordered phase with increasing density and decreasing noise.

*r.negi@fz-juelich.de

†rg_winkler@gmx.de

‡g.gompper@fz-juelich.de

Another class of models emphasizes the short-range steric repulsion, and possibly longer-range attraction between the self-propelled units, called active Brownian particles (ABPs). This implies that the shape of the objects is now relevant to determine structure formation and collective motion. Motility-induced phase separation is observed in such systems, where uniformly distributed spherical ABPs can phase separate into a dense phase of slow-moving particles and dilute fast-moving particles for certain packing fractions and activities [27–30], while ABPs with elongated shapes form nonequilibrium motile clusters and swarm [31–33].

Models just based on an attraction of individual units to the center of mass of neighboring particles induced by self-steering controlled by visual perception [34–37] display different nonequilibrium structures like clusters, single-file motion, and milling. Simulations of self-propelled particles with repulsive and attractive interactions show the formation of rings, vortexlike swarms, and circular aggregates in two dimensions [38,39], and tori, spherical, shell or cylindrical aggregates in three dimensions, depending on the range and amplitude of the potential [40,41]. Another mechanism, which has been predicted to lead to mobile swarms and milling, is the blockage of the visual perception by nearby particles [7].

Using vision-based velocity alignment with time delays, agents can spontaneously condense into droplets [42] and increasing the activity and/or delay time of an active particle's attraction to a target point can induce a dynamic chiral state [43]. The combination of the two mechanisms of attraction and Vicsek-type alignment [44] yields a shift of the critical noise amplitude of the phase transition, and type of phase transition, compared to the case of pure velocity alignment [19]. Detailed observations of flocks of surf scoters have also been used to infer individual interaction forces in the behavioural zonal model [45].

After the recognition that in starling flocks a typical individual significantly interacts only with seven or eight closest neighbors [11], models with metric-free topological interactions have also been studied [46–49]. For instance, the topological Vicsek model, in which particles align their velocity with neighbors defined through the first Voronoi shell, shows qualitative different results, like no density segregation, compared to its metric counterpart. In Delaunay-based models [48], the communication topology of the swarm is determined by Delaunay triangulation, where the rules of attraction and repulsion between neighboring individuals are the same as for the zone-based models, except that the region of attraction is unbounded. The results suggest that Delaunay-based models are more appropriate for swarms that are larger in number and more spatially spread out, whereas the zone-based models are more appropriate for small groups.

In this article, we focus on the numerical investigation of a minimal cognitive flocking metric model with visual perception [35,37] and polar-based alignment [19] for a system of self-steering particles. The usual ABPs are additionally equipped with visual perception and polar-alignment interactions. The visual signal allows these intelligent ABPs (iABPs) to detect the instantaneous position of the center of mass of neighboring particles within their vision cone (VC), whereas polar alignment favors reorientation toward the average orientation of neighbors. Our model shares some basic features

with the behavioral zonal model [17], like long-range attraction, medium-range alignment, and short-range repulsion. However, it is important to note that in our article, we incorporate (i) hard-core excluded-volume interactions instead of a zone of repulsion between particles [17] or even point particles [35,44], and (ii) a limited maneuverability in response to external signals. Additionally, the vision-based attraction in our model is nonadditive, i.e., the reorientation force does not depend on the number of particles, but their (normalized) distribution in the VC. A recent theoretical study [50] highlights the influence of nonadditive versus additive interactions on structure formation in the Vicsek model. Experimentally, systems of iABPs can be realized by active colloids, which are steered externally by a laser beam, with an input signal mimicking visual perception [51–53].

The main goal of our article is the exploration of the state diagram, which depends on several parameters such as propulsion strength, maneuverabilities for vision-induced steering and alignment, vision angle, and ranges of vision and alignment interactions—as well as a characterization of the emerging structures and dynamical behaviors. We find various types of emergent structures like dispersed clusters, compact aggregates, wormlike swarms, and milling, resulting from the interplay of visual-signal-controlled steering and polar alignment. An important feature is the formation of wormlike swarms with a large variability of elongation and width. The dynamics of the swarms displays a persistent superdiffusive motion over a wide range of timescales, which becomes diffusive at long times. This motion is characterized by a persistence length, controlled by the maneuverabilities and vision angle. Furthermore, swarms are found to display interesting trajectories, with long periods of directed motion interrupted by sharp turns or circular arcs.

II. MODEL

We consider a system of N responsive iABPs with the position $\mathbf{r}_i(t)$ of particle i ($i = 1, \dots, N$) at time t . The particles are self-steered with constant propulsion force $\mathbf{F}_i^a(t) = \gamma v_0 \mathbf{e}_i(t)$ along the direction $\mathbf{e}_i(t)$ and velocity v_0 . The dynamics of this system is governed by the equations of motion [37,54]:

$$m\ddot{\mathbf{r}}_i = -\gamma\dot{\mathbf{r}}_i + \gamma v_0 \mathbf{e}_i + \mathbf{F}_i + \boldsymbol{\Gamma}_i(t). \quad (1)$$

Here, m is the mass of an iABP, γ the translational friction coefficient, and $\mathbf{F}_i = -\partial U(\mathbf{r})/\partial \mathbf{r}_i$ the force due to excluded-volume interactions between the iABPs, which are taken into account by the short-range, truncated, and shifted Lennard-Jones potential

$$U(r) = \begin{cases} 4\epsilon\left(\left(\frac{\sigma}{r}\right)^{12} - \left(\frac{\sigma}{r}\right)^6\right) + \epsilon, & r \leq 2^{1/6}\sigma \\ 0, & \text{otherwise,} \end{cases} \quad (2)$$

where $r = |\mathbf{r}|$ is the distance between iABP particles, σ represents their diameter, and ϵ is the energy determining the strength of repulsion. The force \mathbf{F}_i describes fluctuations and is modeled as a stochastic Gaussian and Markovian process of zero mean and the second moments $\langle \boldsymbol{\Gamma}_i(t) \cdot \boldsymbol{\Gamma}_j(t') \rangle = 2d\gamma k_B T \delta_{ij} \delta(t - t')$ in d dimensions, with T the temperature and k_B the Boltzmann constant.

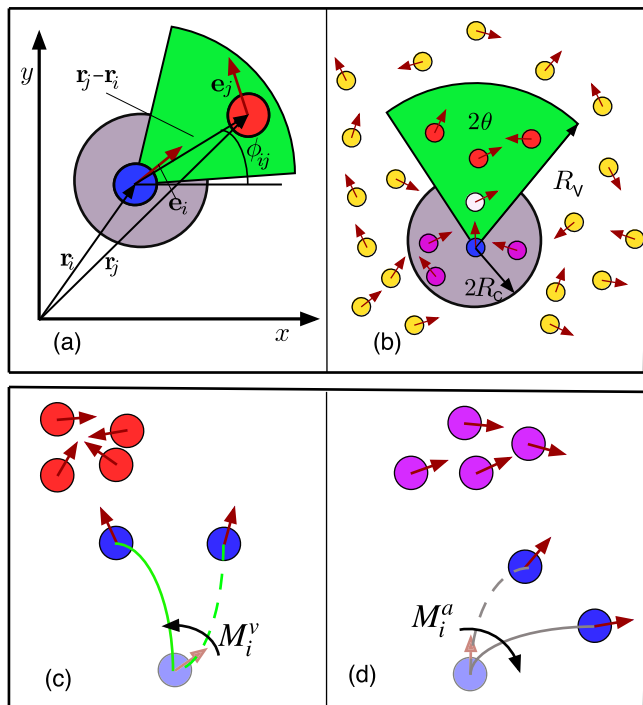


FIG. 1. (a) Schematic representation of vision cone and alignment neighborhood of particle i at position \mathbf{r}_i , with orientation \mathbf{e}_i , distance vector $\mathbf{r}_j - \mathbf{r}_i$ to other particles, and the corresponding orientation angle ϕ_{ij} . (b) Polar orientation field with cutoff R_C and vision cone of a particle (blue) with vision angle θ and vision range R_V . This particle interacts with other particles (red) through visual perception only within the vision cone (green) and aligns with other particles (pink) within the alignment region (grey). Particles (white) in the overlap region contribute to both interactions. (c) Steering behavior of an iABP as influenced by adaptive vision-induced torque M_i^v , depicted for weak (dashed green trajectory) and strong (full green trajectory) maneuverability Ω_v . (d) Steering behavior of an iABP as determined by the alignment-induced torque M_i^a , illustrated for weak (dashed grey trajectory) and strong (full gray trajectory) maneuverability Ω_a .

An iABP is able to react to information about the position and orientation of neighboring particles. As shown schematically in Fig. 1, particle i at position \mathbf{r}_i can adjust its propulsion direction \mathbf{e}_i through self-steering in the direction $\mathbf{u}_{ij} = (\mathbf{r}_j - \mathbf{r}_i)/|\mathbf{r}_j - \mathbf{r}_i|$, determined by the positions of neighbors, with an adaptive torque M_i^v , as in the cognitive flocking model [9,35,37]. Simultaneously, it is capable to align its propulsion direction with neighboring particles, \mathbf{e}_j , with the alignment torque M_i^a , similar to the Vicsek model [5,21,50]. Hence, the dynamics of the propulsion direction of particle i is determined by [55]

$$\dot{\mathbf{e}}_i(t) = M_i^v + M_i^a + \mathbf{A}_i(t) \times \mathbf{e}_i(t). \quad (3)$$

Here, the \mathbf{A}_i represent Gaussian and Markovian stochastic processes with zero mean and the correlations $\langle \mathbf{A}_i(t) \cdot \mathbf{A}_j(t') \rangle = 2(d-1)D_R\delta_{ij}\delta(t-t')$, with the rotational diffusion coefficient D_R .

The vision-induced torque is given by

$$\mathbf{M}_i^v = \frac{\Omega_v}{N_{c,i}} \sum_{j \in \text{VC}} e^{-r_{ij}/R_0} \mathbf{e}_i \times (\mathbf{u}_{ij} \times \mathbf{e}_i), \quad (4)$$

with the visual maneuverability Ω_v and the number

$$N_{c,i} = \sum_{j \in \text{VC}} e^{-r_{ij}/R_0} \quad (5)$$

of iABPs within the VC. The condition for particles j to lie within the VC of particle i is

$$\mathbf{u}_{ij} \cdot \mathbf{e}_i \geq \cos(\theta), \quad (6)$$

where θ —denoted as vision angle in the following—is the opening angle of the VC centered by the particle orientation \mathbf{e}_i (Fig. 1). In addition, we limit the vision range to a distance R_V , i.e., $|\mathbf{r}_i - \mathbf{r}_j| \leq R_V$, and treat all particles further apart as invisible. It is important to note that the additional exponential distance dependence in Eq. (4), with a characteristic range $R_0 < R_V$, becomes only relevant when several particles are present in the VC, because for a single particle the exponential dependence is canceled out due to its simultaneous presence in the numerator and denominator. At higher local particle densities, it implies that mainly the nearest neighbors contribute to the visual perception, which can be interpreted as a blocking of the view on the more distant particles by the nearest neighbors. We employ $R_V = 4R_0$ in our simulations.

Steering due to alignment of the propulsion direction (velocity alignment) is described by the adaptive torque

$$\mathbf{M}_i^a = \frac{\Omega_a}{N_{a,i}} \sum_{j \in \text{PA}} \mathbf{e}_i \times (\mathbf{e}_j \times \mathbf{e}_i), \quad (7)$$

with the alignment maneuverability Ω_a , and the number $N_{a,i}$ of iABPs in the polar-alignment circle (PA) (Fig. 1). The condition for particles j to lie within the polar alignment (PA) range of particle i is $|\mathbf{r}_i - \mathbf{r}_j| \leq 2R_c$, where R_c is the cutoff radius. Unless stated otherwise, $R_c = \sigma$, i.e., particles align up to the second shell of neighbors. Particles inside the overlap zone of the VC and PA regions interact both via M_i^v and M_i^a .

In the following, we focus on a two-dimensional system, where the propulsion directions in polar coordinates are given by $\mathbf{e}_i = (\cos \phi_i, \sin \phi_i)^T$ (see Fig. 1), and yield the equations of motion for the orientation angles ϕ_i ,

$$\begin{aligned} \dot{\phi}_i = & \frac{\Omega_v}{N_{c,i}} \sum_{j \in \text{VC}} e^{-r_{ij}/R_0} \sin(\phi_{ij} - \phi_i) \\ & + \frac{\Omega_a}{N_{a,i}} \sum_{j \in \text{PA}} \sin(\phi_j - \phi_i) + \Lambda_i(t). \end{aligned} \quad (8)$$

The first sum on the right-hand side of Eq. (8) describes the preference of an iABP to move toward the center of mass of iABPs in its VC, while the second sum describes the preference of an iABP to align with the neighboring particles. In the vision-based self-steering, the sum corresponds to the projection of the positions of all N_c particles within the VC onto the “retina” of particle i , with ϕ_{ij} the polar angle of the unit vector $\mathbf{u}_{ij} = (\cos \phi_{ij}, \sin \phi_{ij})^T$ between the positions of particles i and j . The parameters Ω_v and Ω_a are denoted “maneuverabilities” because the particle can react more quickly

TABLE I. Summary of key model parameters. For details, see text.

Parameter	Description
Pe	Péclet number
θ	vision angle
Ω_v	visual maneuverability
Ω_a	alignment maneuverability
Φ	packing fraction
R_0	high-local-density vision range
R_V	low-local-density vision range
R_C	polar alignment radius

to external cues by changing its orientation, i.e., it becomes more maneuverable, for larger values of Ω_v and Ω_a , compare Fig. 1(c) and 1(d). The activity of the iABPs is characterized by the Péclet number

$$\text{Pe} = \frac{\sigma v_0}{D_T}, \quad (9)$$

where $D_T = k_B T / \gamma$ is the translational diffusion coefficient. Here, the Péclet number represents the ratio of times spent in advective and diffusive motion. The key parameters of our model are summarized in Table I.

Our model presents a minimalistic description of self-steering particles with visual perception and velocity alignment, and provides insight into the interplay of these two swarming models. However, it depends on a significant number of parameters, as there are the Péclet number Pe, the vision angle θ and the vision range R_0 , the visual maneuverability Ω_v , the alignment maneuverability Ω_a , the particle size σ , and the packing fraction Φ . In order not to get lost in this large parameter space, we focus here varying the alignment-vision ratio Ω_a/Ω_v , the Péclet number Pe, and the vision angle θ .

III. PARAMETERS

In the simulations, we measure time in units of $\tau = \sqrt{m\sigma^2/(k_B T)}$, energies in units of the thermal energy $k_B T$, and lengths in units of σ . We choose $\gamma = 10^2 \sqrt{mk_B T}/\sigma^2$ and the rotational diffusion coefficient $D_R = 8 \times 10^{-2}/\tau$, which yields the relation $D_T/(\sigma^2 D_R) = 1/8$. The above choice of the friction and rotational diffusion coefficients ensures that inertia does not affect the behavior, because the resulting relation $m/\gamma = 10^{-2}\tau \ll \tau$ implies strongly overdamped single-particle dynamics. The main reason for including the inertia term in Eq. (1) is the reduced numerical effort and the improved accuracy of the numerical integration of Eq. (1), as purely Brownian dynamics requires an orders of magnitude smaller time step. We set $\epsilon/k_B T = (1 + \text{Pe})$ to ensure a nearly constant iABP overlap upon collisions, even at high activities. The iABP density is measured in terms of the global packing fraction $\Phi = \pi\sigma^2 N/(4L^2)$, with L the length of the quadratic simulation box. Periodic boundary conditions are applied, and the equations of motion Eq. (1) are solved with a velocity-Verlet-type algorithm suitable for stochastic systems, with the time step $\Delta t = 10^{-3}\tau$ [56]. We perform 10^7 equilibration steps and collect data for additional 10^7 steps. For certain averages, up to ten independent realizations are considered.

As shown in Ref. [57], for the ratio $M = mD_R/\gamma = 8 \times 10^{-4}$ and the considered Péclet numbers, we do not expect MIPS.

If not indicated otherwise, the number of particles is $N = 625$, the length of the simulation box is $L = 250\sigma$, corresponding to a packing fraction $\Phi = 7.85 \times 10^{-3}$, the characteristic radius is $R_0 = 1.5\sigma$, $\Omega_v/D_R = 12.5$, and the vision angle is $\pi/16 \leq \theta \leq \pi$.

Initially, the iABPs are typically arranged on a square lattice, with iABP distances equal to their diameter σ , in the center of the simulation box. To study the importance of vision and alignment in the interplay between these two self-steering mechanisms, we keep the vision-based maneuverability Ω_v/D_R constant and vary the alignment-vision ratio by changing the alignment-based maneuverability Ω_a .

IV. RESULTS

A. Phases and phase diagram

1. Phase behavior—vision-induced steering versus polar alignment

The effect of the maneuverability ratio of polar alignment and vision-induced steering, Ω_a/Ω_v , and of the vision angle on the emerging structure is illustrated in Fig. 2 for two Péclet numbers. The packing fraction $\Phi = 0.00785$ is very low, hence, typically only a single or very few clusters or aggregates can be observed at any moment in time.

For the low Péclet number $\text{Pe} = 10$, where orientational noise plays a significant role, the state diagram in Fig. 2(a) shows two clearly distinguishable regimes: (i) the pursuit-dominated regime at low $\Omega_a/\Omega_v \lesssim 4$ and large vision angles $\theta \gtrsim \pi/4$, characterized by large quasicircular, nearly immobile clusters, and (ii) the alignment-dominated regime at higher $\Omega_a/\Omega_v \gtrsim 10$ and smaller vision angles $\theta \lesssim \pi/5$, characterized by thick elongated wormlike swarms, which are highly mobile.

When alignment interactions dominate, $\Omega_a/\Omega_v \gtrsim 10$, the iABPs obviously tend to align in the same direction, but cohesion by vision-based steering toward clusters of other iABPs is still relevant; together, these two effects result in the formation of wormlike motile swarms for large vision angle $\theta = \pi$. As the vision angle is reduced to $\pi/5$, the number of particles in the VC decreases, thus, cohesion weakens, and the wormlike swarms become thinner and more elongated. An important point to note is that even for very small vision angles, i.e., $\theta \leq \pi/8$, vision-based cohesion remains important for aggregate formation due to the very low packing fraction.

When the vision-mediated interaction dominates, i.e., for $\Omega_a/\Omega_v = 0.1$ and 0.5, close-packed structures are observed for the vision angle $\theta \geq \pi/3$, and dilute structures for the lower angle $\theta \leq \pi/6$. These cases are similar to those of systems with purely vision-based interactions [37]. For large vision angles, a significant number of neighbors are sensed by an iABP, which then moves toward their center of mass easily, the effect of the alignment interaction is too weak to generate any significant parallel orientation and the iABPs form large close-packed aggregates. When the vision angle is low, e.g., $\theta = \pi/6$, very few particles are detected within the VC, no clusters can form, and particles are distributed homogeneously.

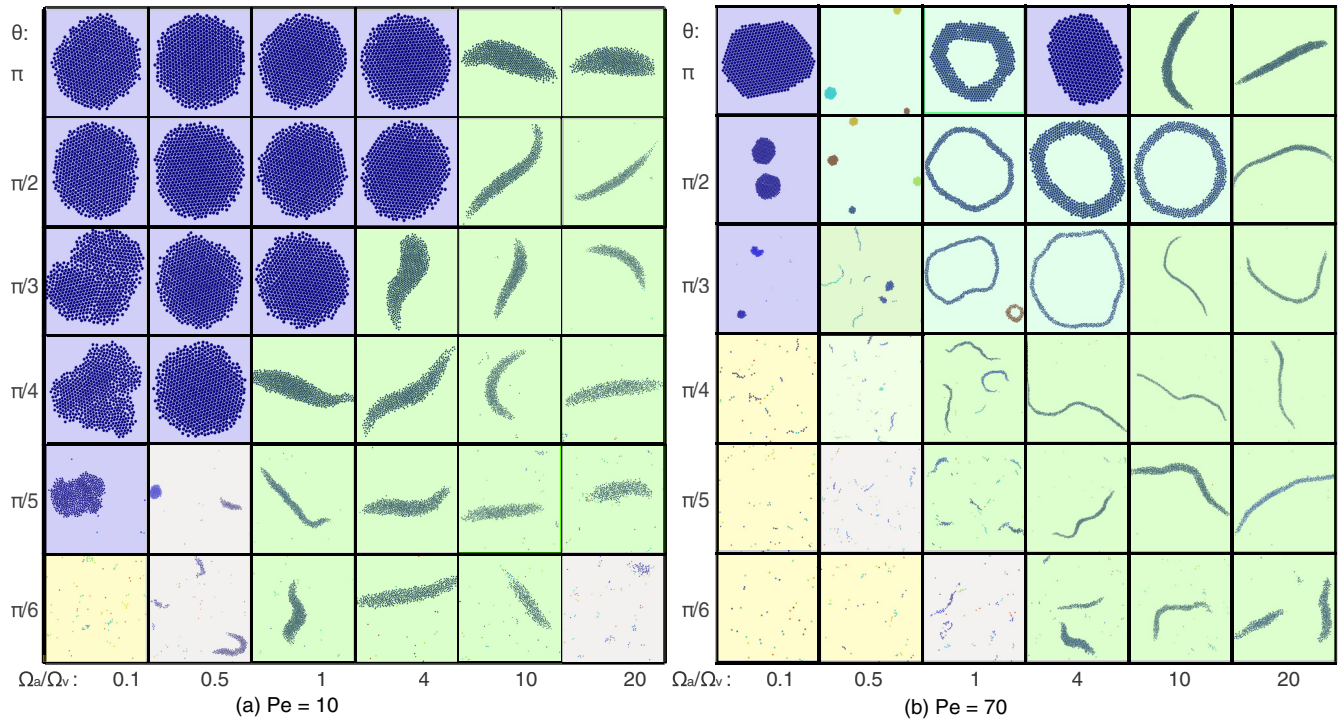


FIG. 2. Snapshots of emerging structures for various vision angles θ , alignment-vision ratios Ω_a/Ω_v , and the Péclet numbers (a) $Pe = 10$ and (b) $Pe = 70$. To ensure clear visibility, the snapshots are not presented to scale. For certain structures, a zoomed-in view is necessary to provide a more detailed representation, see Fig. 14 (Appendix A) for scaled structures. The dilute phase is highlighted within a yellow box, dispersed clusters are represented in grey boxes, close-packed clusters in purple boxes, and wormlike swarms in green boxes. See also movies M1–M6 [58].

For intermediate values $\Omega_a/\Omega_v = 4$, close-packed structures are observed at the high vision angle $\theta = \pi$, while thick wormlike motile swarms emerge at the lower value $\theta = \pi/3$ (see also movies M1 and M2 [58]).

The effect of vision-based steering becomes weaker with decreasing vision angle, as fewer particles appear in the VC. This can be captured by an effective maneuverability $\Omega_{v,\text{eff}} = \Omega_v \theta^\nu$ with $\nu \geq 1$. We will show below that $\nu \simeq 2$. Thus, vision-based steering dominates at large vision angles, resulting in compact clusters and alignment for intermediate vision angles, which favors wormlike swarms. The wiggling of the wormlike swarm arises from the orientational noise of the leading particles.

For the higher Péclet number $Pe = 70$, where persistent ballistic motion becomes more prevalent, the characteristic emergent structures are displayed in Fig. 2(b). At high alignment-vision ratio, again elongated wormlike swarms are observed, which are, however, much thinner compared to those of the lower activity case with $Pe = 10$. Another feature is the emergence of milling structures, where thin wormlike swarms “bite their own tail” and form ringlike rotating aggregates; they are observed for $1 \leq \Omega_a/\Omega_v \leq 10$, and vision angles $\pi/3 \leq \theta \leq \pi/2$ (see also movie M3 [58]). In the vision-dominated regime, with $\Omega_a/\Omega_v = 0.5$, we observe small rotating clusters or a coexistence-phase with small wormlike swarms and small rotating aggregates at the vision angle $\theta \geq \pi/3$ (see also movies M4 and M5 [58]). A phase of small wormlike swarms is found for $\theta \leq \pi/4$, which is similar to the worm-aggregate phase and single-file motion

in the system without alignment interactions [37], except that the aggregates here are rotating and are smaller in size. We would like to emphasize that we use different initial conditions for all parameter sets to avoid a bias by the initial condition toward some rare configuration, in particular, for the milling structures. The highly elongated wormlike swarms can sometimes show milling intermittently, but then regain the wormlike conformation (see also movie M6 [58]). Yet, the milling conformations displayed in Fig. 2(b) always remain stable over the whole simulation time. For close-packed structures at $Pe = 10$ in Fig. 2(a), we employ an initial configuration, where particles are distributed uniformly. This leads first to the formation of multiple close-packed aggregates, which subsequently merge to form a single large cluster. A different behavior is observed for the small rotating aggregates at $Pe = 70$, e.g., at $\Omega_a/\Omega_v = 0.5$ and $\theta \geq \pi/3$ in Fig. 2(b), which do not merge but rather form by splitting of an initial large aggregate in the center of the simulation box. Thus, the small rotating clusters at high activities are different from the large close-packed aggregates observed at lower activities.

2. Phase behavior—alignment-dominated regime

For a more detailed investigation of the alignment-dominated regime, we focus on the alignment-vision ratio $\Omega_a/\Omega_v = 10$. This provides insight into the structural evolution with increasing activity, characterized by the Péclet number Pe and the vision angle θ . Figure 3 shows typical

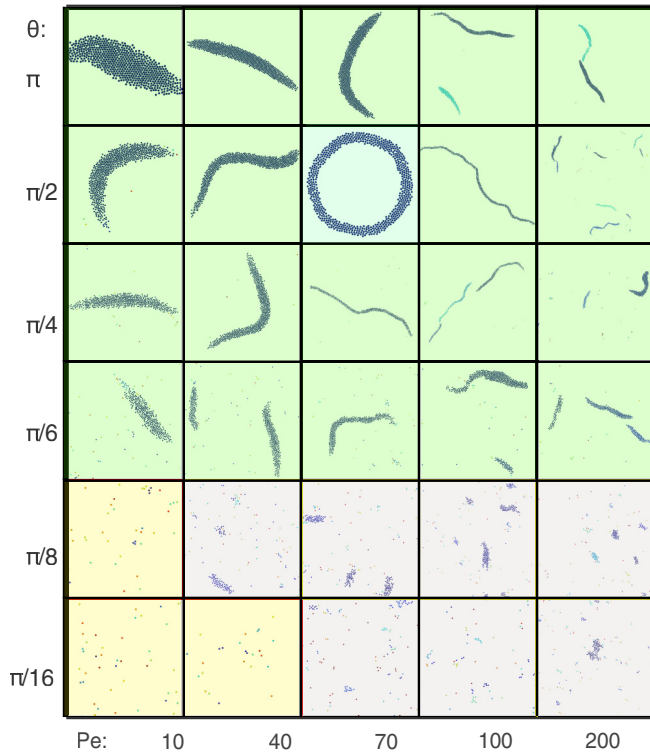


FIG. 3. Snapshots of iABP structures for various vision angles θ , Péclet numbers Pe , and the alignment-vision ratio $\Omega_a/\Omega_v = 10$. The snapshots are not to scale for better visualization. See Fig. 15 for a full phase diagram.

snapshots of emerging structures, like thin and thick wormlike swarms, milling, dispersed clusters, and a dilute phase as a function of these two parameters. For large vision angles $\theta \geq \pi/4$, predominately long and thick motile wormlike swarms are present. For vision angles $\theta \leq \pi/6$, either dilute or dispersed clusters dominate.

With increasing propulsion, the large wormlike swarms become thinner and more elongated as long as $\theta \gtrsim \pi/4$, while for $\theta \leq \pi/8$ small aggregates persist. At high activity, $Pe \geq 100$, the large swarms show dynamical splitting into multiple swarms, while small swarms can merge into larger swarms. The very thin wormlike swarms can sometimes span the whole system. There is a small window of parameters ($Pe \simeq 70$, $\theta \simeq \pi/2$), where circular millinglike structures appear.

3. Phase behavior—balanced alignment-vision regime

Figure 2 indicates that $\Omega_a/\Omega_v = 4$ roughly marks the boundary between stationary close-packed compact structures—where vision-based attraction dominates—and motile wormlike swarms—where alignment interactions dominate. Thus, these two types of interactions approximately balance each other at this alignment-vision ratio.

Snapshots of typical emerging structures at different Pe and vision angles θ are displayed in Fig. 4. For vision angles $\theta \leq \pi/8$, either dilute or dispersed cluster are obtained across all activities. With increasing vision angle $\theta \geq \pi/6$, first wormlike swarms, then compact clusters are stabilized. For higher

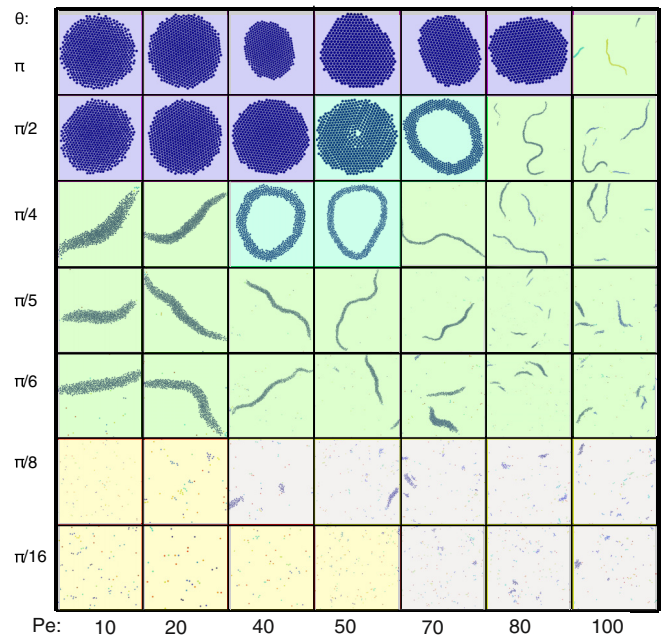


FIG. 4. Snapshots of emerging structures for different activities Pe , vision angles θ , and the alignment-vision ratio $\Omega_a/\Omega_v = 4$ for the packing fraction $\Phi = 0.00785$. The snapshots are not to scale for better visualization.

activity, $Pe \geq 100$, the close-packed structures are absent even at the maximum possible vision angle $\theta = \pi$, because the turning radius of a particle, determined by $Pe/(\Omega_v/D_R)$ [55], becomes too large for fixed maneuverability at high Pe to reach the target cluster. There is a transition from close-packed clusters to thick elongated wormlike swarms at $Pe = 10$ and 20 when the vision angle decreases from $\theta = \pi$ to $\pi/6$, similar to Fig. 2(a). At intermediate activities, $Pe = 40$ to 70 , and intermediate vision angles $\pi/2 \geq \theta \geq \pi/4$, milling structures appear, which are also present at $\Omega_a/\Omega_v = 1$ and 10 for $Pe = 70$ [compare Fig. 2(b)].

The full phase diagram is shown in Fig. 5, where the boundaries between the various phases are clearly delineated. The comparison of Figs. 4 and 5 shows a remarkable feature of the milling structures; as the boundary to the close-packed clusters is approached, the milling band fills more and more in the interior, and at $\theta = \pi/2$ and $Pe = 50$ becomes a milling disk.

4. Discussion

Figures 2–5 together provide an overview of the emerging structures in the three-dimensional parameter space of Pe , θ , and Ω_a/Ω_v .

The main characteristics are the presence of (i) compact clusters in the vision-induced steering regime, with $\Omega_a/\Omega_{v,\text{eff}} \leq 4$, where alignment plays a minor role, (ii) wormlike swarms in the alignment-dominated regime, with $\Omega_a/\Omega_{v,\text{eff}} \geq 10$, where the elongation of the swarm increases and the thickness decreases with increasing Pe and increasing $\Omega_a/\Omega_{v,\text{eff}}$, and (iii) milling at intermediate values of $\Omega_a/\Omega_{v,\text{eff}}$ and Pe .

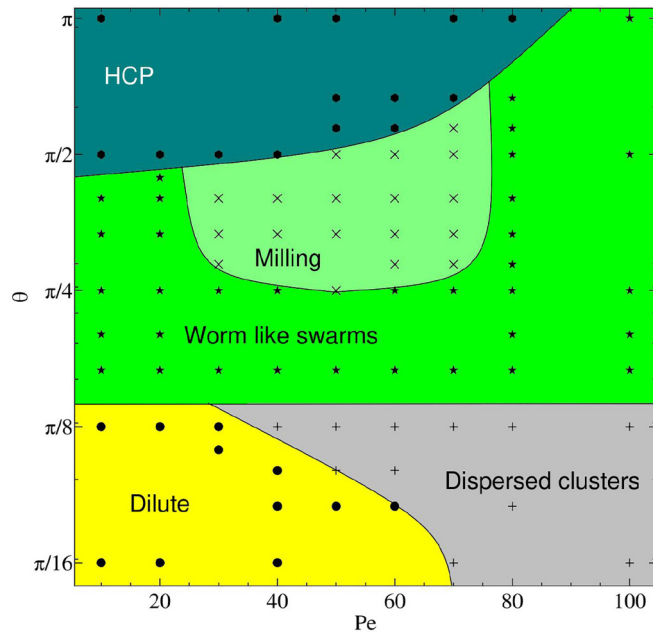


FIG. 5. $Pe - \theta$ phase diagram for $N = 625$, the ratio $\Omega_a/\Omega_v = 4$, the visual maneuverability $\Omega_v/D_R = 12.5$, and the packing fraction $\Phi = 0.00785$. The individual phases are indicated by different colors and symbols: Hexagonally close packed (HCP): navy \bullet , worm: green \star , dilute: yellow \bullet . The lines at the phase boundaries are guides to the eye.

The transition from close-packed aggregates to thick wormlike swarms occurs as the effective alignment-vision ratio increases from $\Omega_a/(\Omega_v\theta^v) \simeq 1$, both with increasing Ω_a (see Fig. 2)—due to stronger alignment—as well as decreasing vision angle (see Fig. 4)—due to weaker vision-induced steering.

Long and thin wormlike swarms are favored by larger activities due to a larger inward-pushing force of particles at the swarm edges, as studied and explained in more detail in Sec. IV B 1 below. Long and thin wormlike swarms are also favored by small vision angles, as the thickness is related to the range $R_0\theta$ of the VC. If the swarm thickness becomes larger than $R_0\theta$, particles on the rim cannot see the full swarm width and the swarm can split, similar to the single-file motion observed in the vision-only case [35,37].

Importantly, alignment stabilizes persistent swarm motion (compared to the single-file motion of vision-only systems [37]) because the incipient leader particle becomes aware of and is affected by its followers.

It is important to note that the presence of wormlike swarms in our model at the low packing fraction ($\Phi = 0.00785$) is in stark contrast to the structures observed in the Vicsek model at higher packing fraction (e.g., $\Phi = 0.25$), where homogeneous disorder phases and giant motile aggregates coexisting with a dilute gas of single particles are observed [21]. Increasing the field of vision yields a comparable outcome to enhancing the visual maneuverability of particles (see Appendix B). Similarly, extending the range of polar alignment demonstrates an effect akin to improving alignment-related maneuverability (see Appendix C).

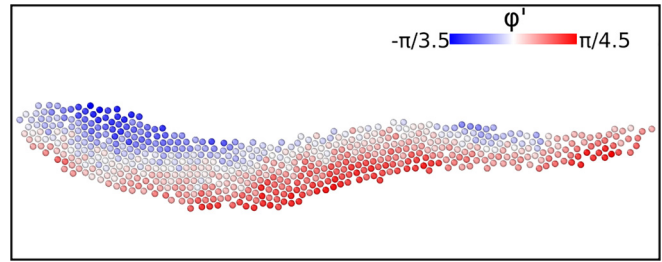


FIG. 6. Snapshot of a wormlike swarm, where particles are colored according to the orientation with respect to the average orientation at $Pe = 40$, $\Omega_a/\Omega_v = 10$, and $\theta = \pi/2$.

B. Structural properties

1. Internal structure of wormlike swarms

An interesting feature of wormlike swarms is the increasing elongation and thinning with increasing Ω_a and increasing Pe . This is related to the behavior of particles at the edge of the swarm, which, due to the vision-induced steering, push inwards but, due to the strong alignment, can do so only to a limited extent. The balance of vision-induced steering and alignment torque can be employed in a simple mean-field estimate (see Appendix D) to predict the particle orientation angle φ^* at the edge of the swarm, with

$$\varphi^* = \pm\theta \left[1 + \frac{\Omega_a}{\Omega_v} \frac{\theta \sin(\theta)}{1 - \cos(\theta)} \right]^{-1}. \quad (10)$$

This estimate is in semiquantitative agreement with the orientational structure of snapshots of wormlike swarms; see Fig. 6.

The preferred tilt angles φ^* imply a lateral compressive force and an equivalent perpendicular Péclet number,

$$Pe_{\perp} = Pe \sin \varphi^*, \quad (11)$$

which increases with Pe , in agreement with the conformations in Fig. 3. Furthermore, the snapshot shows that there is an interesting correlation of particle orientation and local curvature of the swarm centerline, where an imbalance of particles with inward orientation on the two sides seems to generate the snakelike motion of the swarm.

2. Swarm shape and asphericity

We characterize the overall size and shape of the emerging structures by the radius-of-gyration tensor [59]

$$G_{mn} = \frac{1}{N} \sum_{i=1}^N \Delta r_{i,m} \Delta r_{i,n}, \quad (12)$$

where Δr_i is the distance of the i th particle from a cluster's center of mass, $m, n \in \{x, y\}$, and N is the total number of particles in the cluster. We use a distance criterion to define a cluster, where an iABP belongs to a cluster when its distance to another iABP is within a radius of σ_0 . Since our system is very dilute, we choose $\sigma_0 = 2\sigma$. To avoid averages to be strongly affected by configurations which occur only rarely, we only consider realizations which appear in more than 1% of the recorded configurations.

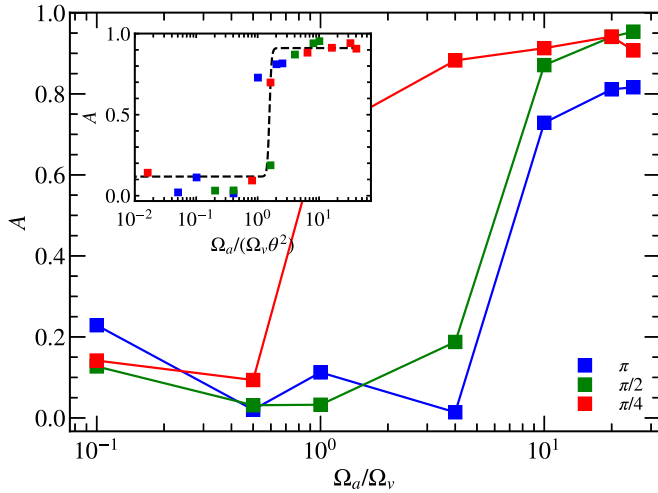


FIG. 7. Aggregate asphericity A as a function of the alignment-vision ratio Ω_a/Ω_v for $Pe = 10$ and the indicated vision angles.

An important quantity to characterize the shape of aggregates is the asphericity

$$A = \frac{|\lambda_1 - \lambda_2|}{\lambda_1 + \lambda_2}, \quad (13)$$

where λ_1 and λ_2 are the eigenvalues of the radius-of-gyration tensor. Figure 7 shows the asphericity A as a function of alignment-vision ratio at various vision angles θ . The close-packed structures for weak alignment and strong vision at small $\Omega_a/\Omega_v \leq 0.5$ are nearly circular, hence, $A \simeq 0$, similar to the vision-only case [37]. The wormlike swarms for $10 \leq \Omega_a/\Omega_v \leq 25$ and $\theta = \pi$, as well as $\Omega_a/\Omega_v = 1$ for $\theta = \pi/4$, are highly elongated, which results in the large asphericities $A \simeq 0.8$. The asphericity starts to increase with Ω_a/Ω_v significantly earlier for smaller vision angles, because cohesion and thus formation of compact aggregates is suppressed for smaller visual signals, which favors wormlike swarms.

Thus, the effect of an increase of the vision angle is similar to an enhanced visual maneuverability, because in both cases the tendency of an iABP to steer toward existing clusters increases. Consequently, we recalibrated the visual maneuverability Ω_v by a factor, which increases with the vision angle θ to accommodate this effect. As a result, we can collapse all data of the asphericity for $\theta \leq \pi/4$ onto a single master curve by employing an effective scaled variable $\Omega_a/(\Omega_v \theta^\nu)$, with $\nu \simeq 2$, as demonstrated in the inset of Fig. 7. This shows that the asphericity displays universal behavior as a function of this scaled alignment-vision ratio, with a sharp transition from the compact-cluster to the wormlike swarm phase at $\Omega_a/(\Omega_v \theta^2) \simeq 2$. A similar scaling behavior is found for the radius of gyration, see Appendix E.

3. Global polarization

The global polarization is characterized by the order parameter

$$P = \left\langle \frac{1}{N} \left| \sum_i \mathbf{e}_i \right| \right\rangle, \quad (14)$$

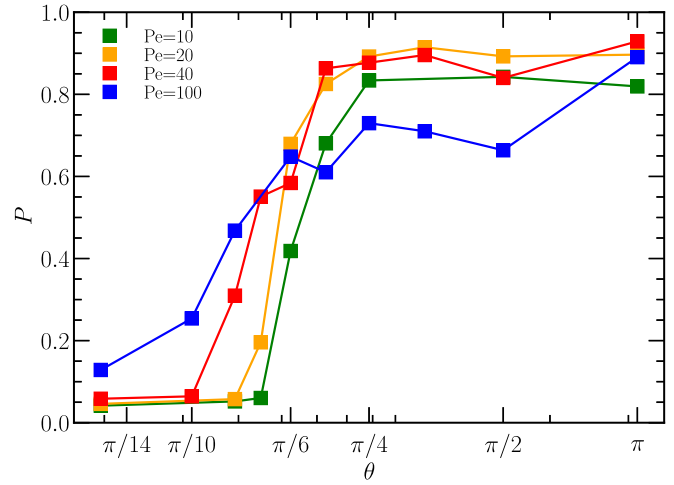


FIG. 8. Polarization order parameter P as a function of the vision angle θ for the indicated activities Pe and $\Omega_a/\Omega_v = 10$. The packing fraction is $\Phi = 0.00785$.

where \mathbf{e}_i is orientation of particle i and the average is performed over time. Figure 8 shows the polarization as a function of the vision angle θ for $\Omega_v/\Omega_a = 10$ at various activities Pe . For $\theta \lesssim \pi/8$, particles are randomly oriented and $P \simeq 0$. For larger vision angles, global polarization emerges, which can reach $P = 1$ for $\theta = \pi$. Global polarization at small vision angles is enhanced by larger Pe , due to more persistent particle motion. It is important to note that we are not characterizing bulk phases here, but typically a single large cluster. Thus, P quantifies the alignment order within the cluster. $P \simeq 1$ also does not imply that the cluster is always moving in the same direction, just that the propulsion directions of the individual particles remain highly aligned at any moment in time. Results for the polarization for $\Omega_v/\Omega_a = 4$, system size $N = 1250$, and various activities Pe are provided in Appendix F.

C. Dynamical properties

1. Mean-square displacement

The translational motion of the iABPs is characterized by their mean-square displacement (MSD)

$$\langle \mathbf{r}^2(t) \rangle = \frac{1}{N} \sum_{i=1}^N \langle (\mathbf{r}_i(t+t_0) - \mathbf{r}_i(t_0))^2 \rangle, \quad (15)$$

where the average is performed over the initial time t_0 . An important reference case is the behavior of single ABPs, for which theoretical calculations in two dimensions yield [1]

$$\langle \mathbf{r}^2(t) \rangle = 4D_T t + \frac{2v_0^2}{D_R^2} (D_R t - 1 + e^{-D_R t}), \quad (16)$$

Figure 9 displays MSDs of iABPs for various alignment-vision ratios, vision angles, and Péclet numbers. For larger $\Omega_a/\Omega_v = 4$ to 25, where alignment interactions dominate over vision-controlled steering (wormlike swarms), the particles move nearly ballistic and $\langle \mathbf{r}^2(t) \rangle \sim t^\alpha$, with the exponent $\alpha \approx 1.95$. For $\Omega_a/\Omega_v \leq 0.1$, in the vision-dominated regime, the close-packed aggregates display translational diffusion

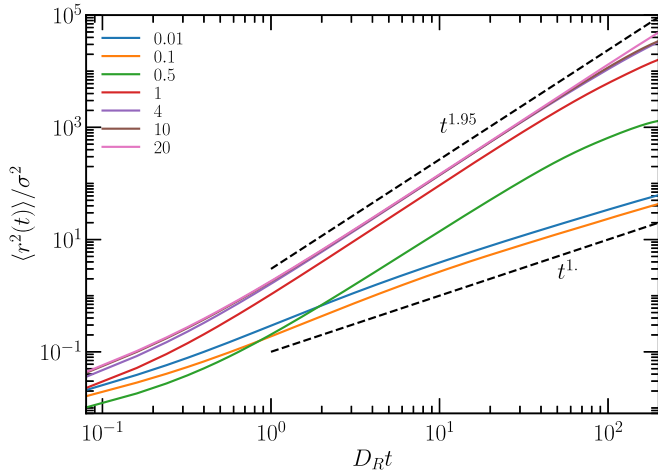


FIG. 9. Mean-square displacement of iABPs as a function of time for $Pe = 10$, $\theta = \pi/4$, and the various indicated ratios Ω_a/Ω_v .

and $\langle r^2(t) \rangle \sim t$. The transition from ballistic diffusive motion occurs at $\Omega_a/\Omega_v \simeq 0.5$ for $\theta = \pi/4$. It shifts to $\Omega_a/\Omega_v \simeq 1$ for $\theta = \pi/2$, in agreement with the conclusion in Sec. IV B 2 that the importance of vision-controlled steering increases with increasing vision angle. Results for the MSD at $Pe = 100$ and $\Omega_a/\Omega_v = 10$ with various vision angles are provided in Appendix G.

2. Collective dynamics

The dynamics of elongated wormlike swarms is characterized by an essentially one-dimensional motion along a curvilinear path, where all particles of the swarm trace out trajectories, which are only slightly displaced laterally from the trajectory of the center-line (see also movie M7 [58]). This is reminiscent of the railway motion performed by semiflexible, tangentially driven active polymers at high Péclet numbers [60].

Thus, we can characterize the dynamics of the whole swarm by the temporal autocorrelation function of individual particles,

$$C_\theta(t) = \frac{1}{N} \sum_{i=1}^N \langle \mathbf{e}_i(t+t_0) \cdot \mathbf{e}_i(t_0) \rangle, \quad (17)$$

where, \mathbf{e}_i represents the orientation of particle i , and N is the total number of particles in the swarm.

In the case of a railway motion, the spatial conformations of the swarm as well as the temporal autocorrelation function, Eq. (17), are determined by the statistical properties of the (infinitely long) rail, with the spatial correlation function of tangent vectors $\mathbf{t}(s)$ (with contour length s)

$$\langle \mathbf{t}(s) \cdot \mathbf{t}(s') \rangle = A \exp(-|s - s'|/\xi_p) \quad (18)$$

and persistence length ξ_p . This length is also the spatial correlation length of shape fluctuations of the center-line of the swarm. Furthermore, the railway assumption implies that

$$\langle \mathbf{e}_i(t+t_0) \cdot \mathbf{e}_i(t_0) \rangle \simeq \langle \mathbf{t}(s) \cdot \mathbf{t}(s+v_0 t) \rangle = A \exp[-(v_0/\xi_p)t], \quad (19)$$

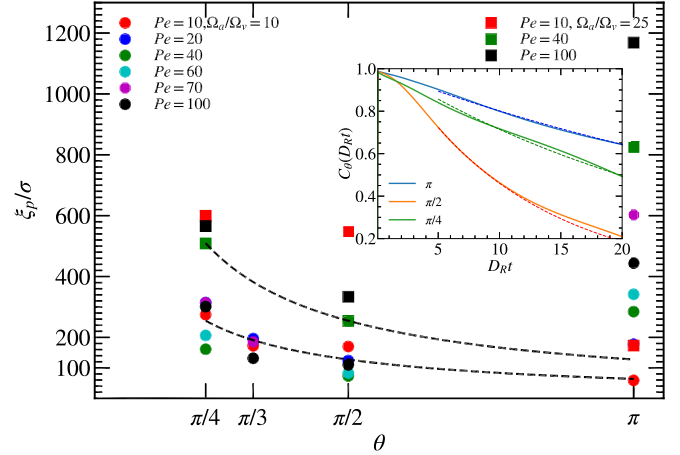


FIG. 10. Persistence length of elongated wormlike swarms as function of the vision angle θ for various Pe and the ratios $\Omega_a/\Omega_v = 10$ (bullets) and $\Omega_v/\Omega_a = 25$ (squares). Inset: Autocorrelation function of the propulsion direction of individual particles at $Pe = 60$ and $\Omega_v/\Omega_a = 10$. Dashed lines are fits.

where v_0 is active velocity. Thus, the temporal decay of $C_\theta(t)$ should be controlled by the relaxation time $\tau = \xi_p/v$, with the *same* persistence length ξ_p as the instantaneous conformations.

Figure 10 shows examples of the autocorrelation function $C_\theta(t)$, together with exponential fits (inset), and the derived persistence lengths for various parameter combinations. It is interesting to note that a comparison of the spatial and the temporal [Eqs. (19) and (H1)] persistence length are in good quantitative agreement for elongated wormlike swarms (see Appendix H). The persistence length ξ_p display three important trends: (i) the persistence grows roughly linearly with the alignment-induced maneuverability Ω_a , (ii) is only weakly dependent on the Péclet number, and (iii) it decreases with the vision angle roughly as a power law θ^{-1} in the range $\pi/4 \leq \theta \leq \pi/2$. Together, this implies

$$\xi_p/\sigma \simeq \Omega_a/(\Omega_v \theta). \quad (20)$$

The increase of the persistent swarm motion (compared to the single-file motion of vision-only systems [37]) with stronger alignment-induced maneuverability can be traced back to the effect of the followers on the incipient leader particle through the (isotropic) alignment interaction. The larger persistence length at $\theta = \pi/4$ than at $\pi/2$ can be attributed to the larger worm length at $\theta = \pi/4$, where a more focused vision enables the particles to more easily follow the incipient leader.

An important point to note here is that the persistence for the considered parameter combinations is always large, with $\xi_p/\sigma > 100$. Since the effective translational diffusion coefficient for a random-walk-like motion with persistence length ξ_p is given by

$$D_T^{\text{eff}} \simeq v_0 \xi_p, \quad (21)$$

this explains the large ballistic/superdiffusive regime in Fig. 9, because the crossover from the ballistic to the diffusion regime occurs at $D_R t^* \simeq D_R \xi_p/v_0$, which implies $D_R t^* \simeq 8(\xi_p/\sigma)/Pe \simeq 100$.

A notable exception in Fig. 10 is the vision angle $\theta = \pi$. In this case, the persistence length increases roughly proportional to the Péclet number. The main difference to the case of smaller vision angles is that the wormlike swarms are here much thicker (and shorter) and exhibit a less persistent motion for small Pe. This implies that the rotational diffusion of the leading group of particles—which is determined by Pe—now plays an important role. Furthermore, with increasing Pe, the swarm thickness decreases (see Fig. 3), which also contributes to an increasing persistence length.

3. Milling

Milling structures are characterized by the angular frequency

$$\omega = \frac{1}{N_e} \frac{|\sum_i (\mathbf{r}_i - \mathbf{r}_{cm}) \times \mathbf{v}|}{\sum_i (\mathbf{r}_i - \mathbf{r}_{cm})^2} \quad (22)$$

and the radius

$$R = \frac{1}{N_e} \sum_i \sqrt{(\mathbf{r}_i - \mathbf{r}_{cm})^2} \quad (23)$$

of these aggregates; here N_e is total number of particles in the milling structure and \mathbf{r}_{cm} is the center-of-mass position.

The radius of the milling ringlike ribbon for $\Omega_a/\Omega_v = 4$ and $\pi/4 < \theta < \pi/2$ increases roughly as $R \sim \text{Pe}^2$. This is caused by the increasing persistence of the iABP motion with increasing Pe. Figure 11(a) shows the scaled radius as a function of the vision angle and suggests that $R \sim \theta^{-\gamma}$, with $\gamma \simeq 1.3$. The angular frequency ω decreases with increasing activity Pe approximately as $\omega \sim 1/\text{Pe}$. This decrease is related to the increasing radius, because $\omega \sim v/R$ and $v \sim \text{Pe}$. Figure 11(b) shows scaled frequency ω as a function of the vision angle, with $\omega \sim \theta^\gamma$ and the same exponent γ as for the radius. Thus, all together, we predict the scaling behavior

$$R = c_R \sigma \theta^{-\gamma} N_e \text{Pe}^2, \quad \omega = c_\omega \theta^{+\gamma} D_R / (N_e \text{Pe}) \quad (24)$$

with $\gamma \simeq 1.3$ and constants c_R and c_ω . The data in Fig. 11 indeed fall very nicely onto these single scaling curves.

D. Finite-size effects

To elucidate the influence of finite-size effects on the presented results, we construct a phase diagram for the same parameters as in Fig. 5 for the alignment-vision ratio $\Omega_a/\Omega_v = 4$, packing fraction $\Phi = 0.00785$, and vision maneuverability $\Omega_v/D_R = 12.5$, but now of twice the number of particles, i.e., $N = 1250$, see Fig. 12. Overall, the topology of the phase diagram remains the same; mostly only phase boundaries are slightly shifted. The most significant change is the extension of the region of stability of the milling structure, which extends to smaller Pe numbers and smaller θ for larger N .

This similarity does not imply that the iABP behavior is independent of N . An obvious effect of increasing N is that the close-packed, nearly circular aggregates in the hexagonally close-packed (HCP) phase grow in size, with their radius increasing as \sqrt{N} . As the particles are all pushing toward the joint center of mass, this implies that the aggregates become more stable, which is

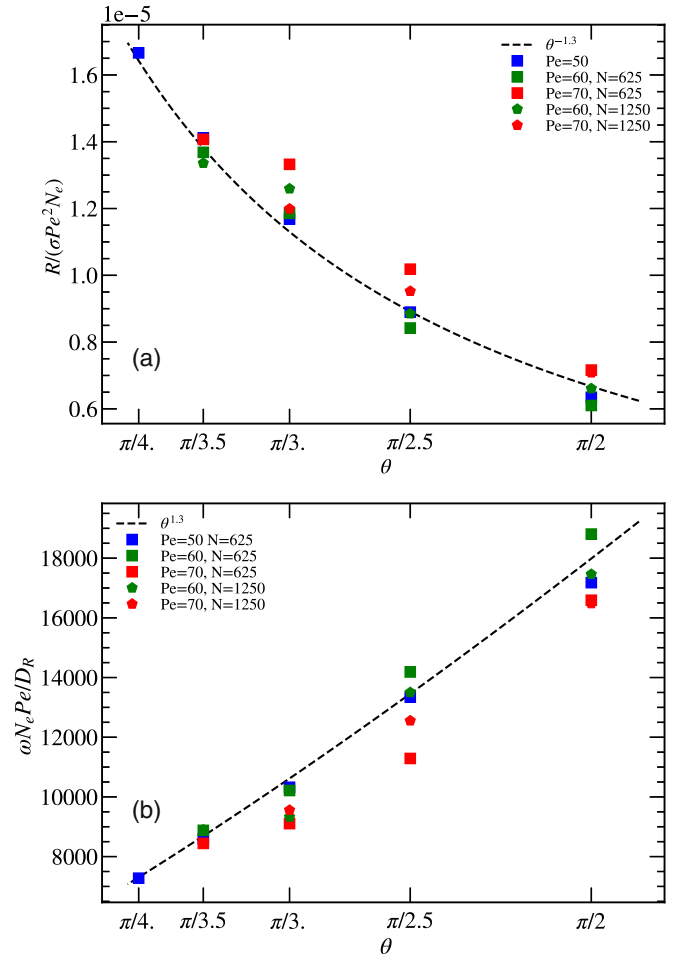


FIG. 11. (a) Scaled radius R and (b) scaled angular frequency ω of milling structure as function of θ at alignment-vision ratio $\Omega_a/\Omega_v = 4$ for various numbers N of iABPs.

expressed by the shift of the HCP: wormlike swarm boundaries to lower vision angles. For the wormlike swarms and milling structures, these can either remain a single aggregate or slit and merge again intermittently into several smaller structures. In the latter case, only minor finite-size effects can be expected. In the former case, increasing N implies longer or thicker wormlike swarms or milling structures. Thicker swarms exhibit a more persistent and less snakelike motion. This also appears for the milling structures, where $R \sim N$ and, correspondingly, $\omega \sim 1/N$, see Fig. 11 and Eq. (24).

V. SUMMARY AND CONCLUSIONS

We have studied the emergent structures and dynamics of ensembles of cognitive, self-steering particles with a combination of visual-perception controlled steering and polar alignment. The visual signal gives particles a tendency to reorient toward the center of mass of other particles in their visual field and implies group cohesion, whereas polar alignment induces particle reorientation toward the average orientation of their neighbors within the alignment-perception range and implies collective directed motion. Depending on the vision-induced maneuverability Ω_v and polar-alignment

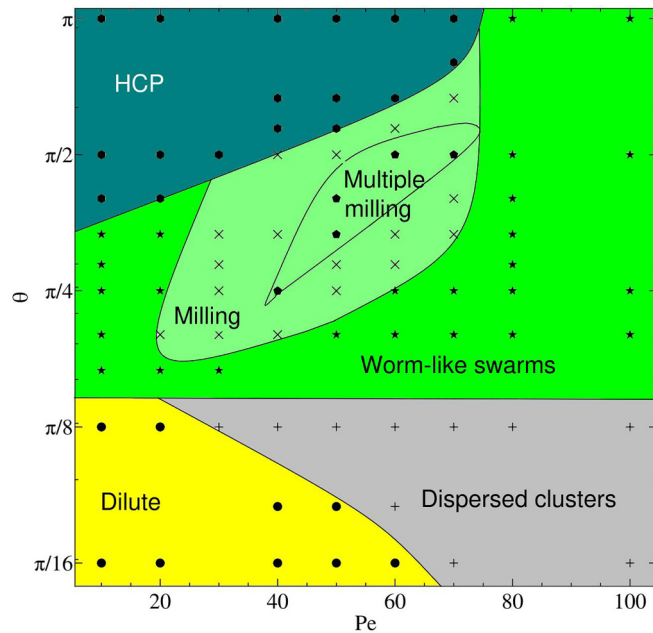


FIG. 12. Phase diagram in Pe - θ space at the particle number $N = 1250$, the alignment-vision ratio $\Omega_a/\Omega_v = 4$, packing fraction $\Phi = 0.00785$, and vision-related maneuverability $\Omega_v/D_R = 12.5$. The individual phases are indicated by different colors and symbols. HCP: navy ●; worm: green ★; dilute: yellow ●. The lines at the phase boundaries are guides to the eye.

related maneuverability Ω_a , various kinds of collective motion are obtained. Moreover, the vision angle θ , the vision range R_θ , and the activity Pe play a crucial role in structure formation. In wormlike swarms, which are predominately observed for large alignment-vision ratios $\Omega_a/\Omega_v \gtrsim 4$, particles move together collectively with little individual orientational fluctuations, and the swarm displays superdiffusive or nearly ballistic motion over long times. Dispersed cluster and dilute phases prevail at small vision angles, typically $\theta \leq \pi/8$, due to the small number of particles in the VC, which implies weak cohesion. Close-packed disklike clusters emerge for high vision-induced maneuverability and vision angle $\theta \geq \pi/4$ because the larger the number of particles in a visible cluster, the larger the tendency to quickly turn toward its center of mass.

Circular milling structures are obtained mainly for balanced alignment-vision ratios, $\Omega_a/(\Omega_v\theta^2) \simeq 4$, at an intermediate range of activities and vision angles. The underlying mechanism for such structures to be stable is that the persistence length of the wormlike contour of a conformation should be on the same order as its contour length because large persistence lengths favor elongated swarms. The milling structure is characterized by a radius $R \sim Pe^2$ and, hence, a rotation frequency $\Omega \sim 1/Pe$. Balanced maneuverability, i.e., $\Omega_a/(\Omega_v\theta^2) \simeq 4$, seems to be a very favorable condition for swarms, in general, because it makes swarms susceptible to external perturbations while remaining cohesive, so that the swarm can quickly react to the appearance of predators. We want to mention parenthetically that the importance of critically in biological systems has also been discussed in the context of scale-free correlation of swarms of midges [61].

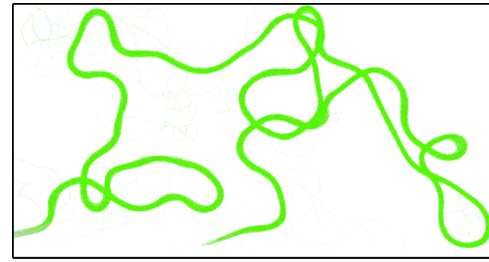


FIG. 13. Typical trajectory of a wormlike elongated swarm at $Pe = 40$, $\theta = \pi/2$, and $\Omega_a/\Omega_v = 10$. See also movie M7 [58].

A closer look at the internal structure of a wormlike swarm reveals interesting features. Particle orientations at the edge of the swarm are weakly inclined toward the centerline, which implies a compressive force responsible for swarm elongation. Furthermore, a lateral asymmetry seems to be correlated with undulations of the centerline.

Although our approach shares some basic features with the boid model [16] and the behavioral zonal model [17], it differs in other important aspects. First, we employ a hard-core repulsion between the agents, which implies close-packed aggregates, whereas the previous models typically adopt a softer repulsion potential, which leads to disordered aggregates. Thus, the way the repulsion between particles is modeled plays a crucial role in structure formation. It certainly depends on the real system to be considered—which of these repulsive interactions is more appropriate. Second, while in other models [16,17] attraction-related reorientation is instantaneous, in our model cohesion emerges from vision-based steering, where the reorientation toward a target is restricted by a limited maneuverability. Thus, both vision- and alignment-related maneuverability are important parameters, which have not been investigated in combination with alignment so far.

Thick wormlike swarms have already been observed in the behavioral zonal model called highly parallel groups [17,18]. However, we also obtain highly elongated, thin wormlike swarms, in particular, for large Péclet numbers and large alignment-vision ratios. These swarms have to be distinguished from the swarms in the pure vision-based minimal cognitive model with and without excluded volume [35,37], where they display single-file motion and are much shorter in length, i.e., less stable. The most interesting feature of these thin worm-like swarms is that they can transform into metastable milling states, where the swarm bites its own tail and then regains the elongated shape later on. Milling structures have also been observed previously in the behavioural zonal model [17]. We observe both large (polar) milling bands and small rotating aggregates—where the latter differ from the nematic ringlike bands in the vision-only case with point particles [35].

Milling has been seen previously in simulations of other models [7,39] but, more importantly, in groups of several animal species in the wild, such as schooling fish [62], army ants [63], bats [64], plant-animal worms [65,66], and dictyostelium [67]. Large extended wormlike swarms have been observed in flocks of birds [6,68], worms (fungus gnat larvae) [69], ducks [70], and more.

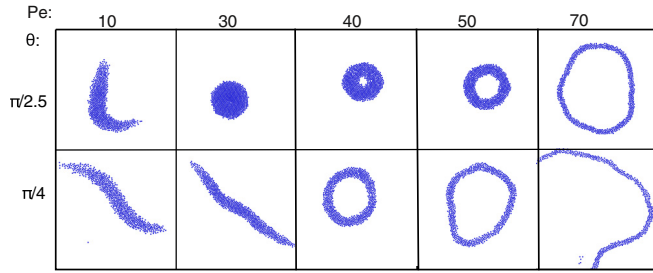


FIG. 14. Snapshots of structures across various activities and two θ values, for $\Omega_a/\Omega_v = 10$, scaled according to the particle size, to demonstrate the increasing size of millings with increasing Pe . This should be compared to Fig. 3, where snapshots are not to scale.

We conclude from our simulations that it would be very interesting to study and characterize the existence, motion, and trajectories of large wormlike swarms in more detail, both in simulations and in animal herds in the wild. We have analyzed the trajectories in terms of a persistent random walk model and extracted an effective persistence length. However, it is not at all obvious that the assumption of a persistent random walk fully captures the complexity of motion of an animal herd. In fact, a more detailed look at the long-time trajectory of a wormlike swarm, see Fig. 13, already indicates that this behavior—with long stretches of persistent directed motion interrupted by looplike pieces and sharp turns—is much more complex and interesting than a simple persistent random walk.

Another interesting perspective and challenge would be to see whether our model would be able to describe the behavior of specific animal groups by matching the model parameters to real systems.

APPENDIX A: SIZE OF SWARMS, MILLING, AND AGGREGATES

The scale of structures in Fig. 3 has been chosen such as to make the window size comparable to the structure size. Thus, these swarms, milling, and aggregates are not to scale. To provide a better understanding of the much larger size of wormlike swarms compared to compact clusters, we display some of the structures again in Fig. 14, now scaled according to the particle size.

APPENDIX B: EFFECT OF VISION RANGE R_0

Figure 15 shows the dependence of the phase diagrams of iABPs on the range R_0 of visual perception, specifically for (a) $R_0 = 1.5\sigma$ and (b) $R_0 = 3.0\sigma$, for a fixed alignment-vision ratio of $\Omega_a/\Omega_v = 10$. With increasing vision range R_0 , the number of particles in the VC increases significantly. As a result, the importance of the vision-induced steering increases with increasing R_0 , which implies an effective reduction of the effect of polar alignment. Thus, the formation of wormlike swarms is enhanced for a smaller vision range, while compact aggregates are favored for a larger vision range.

Interestingly, this effect of an increasing vision range is akin to enhancing the visual maneuverability of the particles. This behavior is similar to an increase of the vision angle, as discussed in Sec IV A 1. It enables a broader scope of particle detection and influences the collective behavior accordingly.

APPENDIX C: EFFECT OF ALIGNMENT RANGE R_c

Figure 16 shows the effect of the alignment range R_c on the phase behavior of iABPs, for two Péclet numbers, $Pe = 40$ and $Pe = 100$, with $\Omega_a/\Omega_v = 4$.

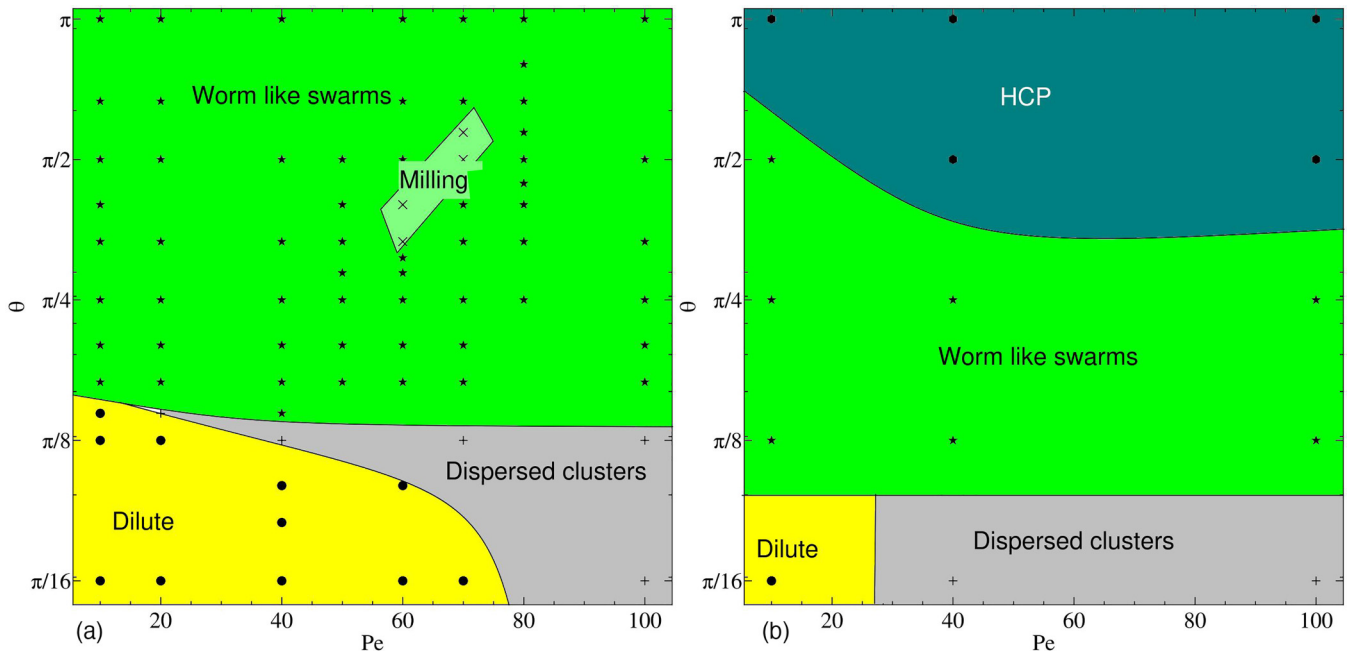


FIG. 15. $Pe - \theta$ phase diagram for the vision range (a) $R_0 = 1.5\sigma$ and (b) $R_0 = 3\sigma$. In both cases, $R_v = 4R_0$. Other parameters are the alignment-vision ratio $\Omega_a/\Omega_v = 10$, packing fraction $\Phi = 0.00785$, number of particles $N = 625$, and visual maneuverability $\Omega_v/D_R = 12.5$. The individual phases are indicated by different colors and symbols. HCP: navy \bullet ; wormlike swarms: green \star ; dilute: yellow \bullet . The lines at the phase boundaries are guides to the eye.

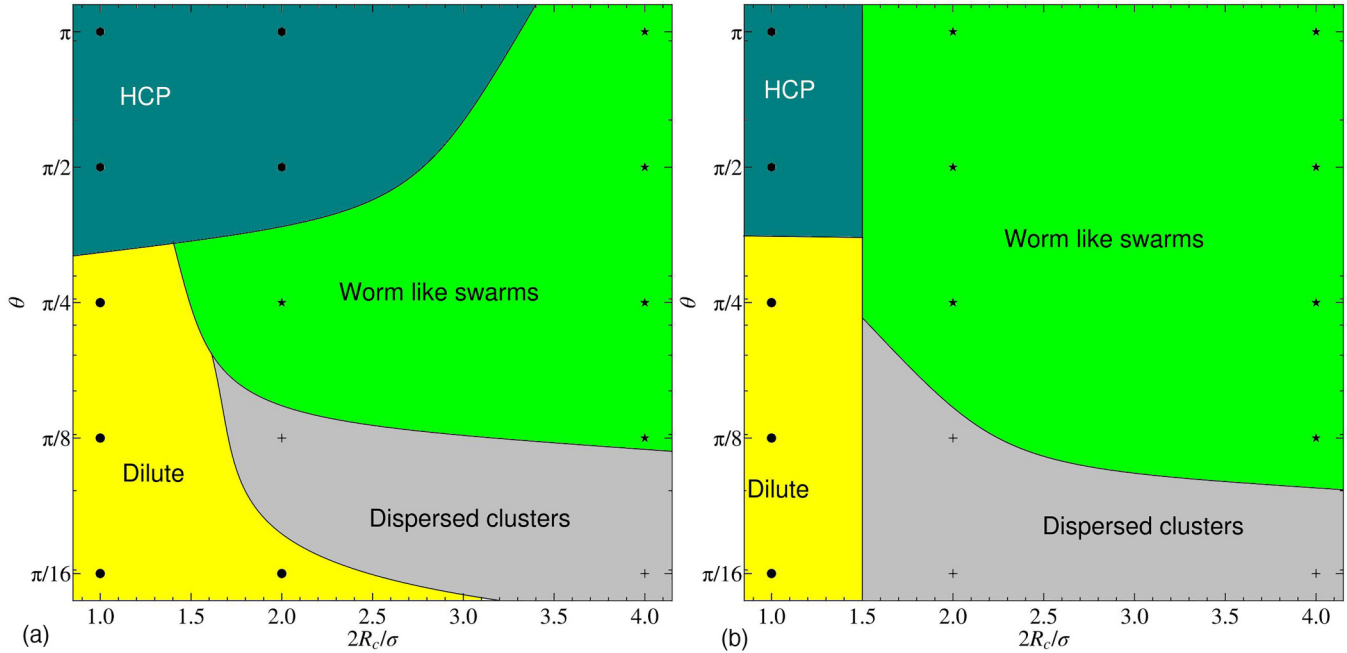


FIG. 16. Phase behavior as a function of the alignment range R_c and the vision angle θ , with (a) $Pe = 40$ and (b) $Pe = 100$ for the maneuverability ratio $\Omega_a/\Omega_v = 4$, vision range $R_0 = 1.5\sigma$, packing fraction $\Phi = 0.00785$, number of particles $N = 625$, and visual maneuverability $\Omega_v/D_R = 12.5$. The individual phases are indicated by different colors and symbols. HCP: navy ●; worm: green ★; dilute: yellow ●. The lines at the phase boundaries are guides for the eye.

When the polar alignment range is small, $R_c = \sigma/2$, the influence of polar alignment is significantly reduced. Only particles within one neighbor shell are present in the alignment region, resulting in the dominance of vision-induced steering. As a consequence, particles tend to form close-packed aggregates for vision angle $\theta \geq \pi/2$, while for $\theta \leq \pi/4$, they form only a dilute phase.

On the other hand, when the range of polar alignment is increased, $R_c = 2\sigma$, a significant number of particles contribute to the polar alignment. This leads to the dominance of polar alignment, resulting in particles forming wormlike swarms at higher vision angles ($\theta \geq \pi/8$), and dispersed clusters at lower angles. Importantly, an increase in the range of polar alignment produces a similar effect as an increase of the alignment-related maneuverability, Ω_a .

APPENDIX D: ORIENTATION OF iABPS AT THE EDGE OF WORMLIKE SWARMS

Equation (8) gives the contribution of visual and alignment torques in polar coordinates. These expressions can be easily evaluated in the two special cases depicted in Fig. 17, when (i) either the particle orientation is perfectly aligned with the preferred direction due to vision [Fig. 17(a)] or (ii) conversely, the direction of motion coincides with the surface tangent [Fig. 17(b)]. In the first case, the visual redirection torque vanishes, $\mathbf{M}_v(\varphi = \theta) = 0$, while the contribution from alignment interaction $\mathbf{M}_a(\varphi = \theta) = \Omega_a \sin(\theta)$ attains a large value. In the second case, the contribution from visual steering is significant, $\mathbf{M}_v(\varphi = 0) = \Omega_v(1 - \cos(\theta))/\theta$, while the contribution from alignment steering vanishes, $\mathbf{M}_a(\varphi = 0) = 0$. In both cases, we assume a uniform distribution of particles within the wormlike swarm. A linear interpolation between

the limiting cases yields

$$\mathbf{M}_v(\varphi) = \Omega_v(\theta - \varphi)(1 - \cos(\theta))\theta^{-2} \quad (D1)$$

and

$$\mathbf{M}_a(\varphi) = \Omega_a \varphi \sin(\theta)\theta^{-1}. \quad (D2)$$

The two steering torques balance each other at the special orientation angle

$$\varphi^* = \theta \left[1 + \frac{\Omega_a}{\Omega_v} \frac{\theta \sin(\theta)}{1 - \cos(\theta)} \right]^{-1}. \quad (D3)$$

For $\Omega_v = 0$, we recover $\varphi^* = 0$, indicating perfect alignment, while for $\Omega_a = 0$, we recover $\varphi^* = \theta$, i.e., perfect alignment along the visual direction. In the limit of small vision angles, $\varphi^* = \theta(1 + 2\Omega_a/\Omega_v)^{-1}$.

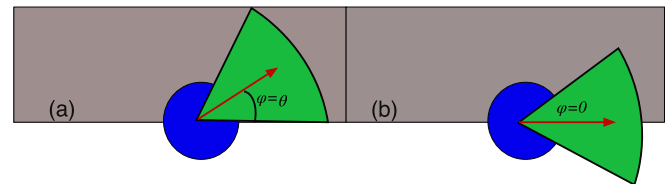


FIG. 17. Particle orientation in the wormlike-swarm phase near the boundary, assuming a uniform distribution of particles within the grey-colored area. (a) Particle pointing along the center of mass (COM) and orientation direction coinciding with the center of the visual field. (b) Particle perfectly aligned along the surface of worm motion.

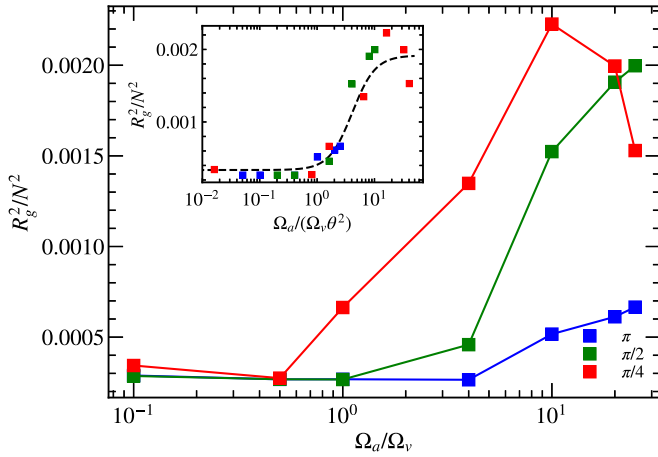


FIG. 18. Radius of gyration as a function of the alignment-vision ratio for $Pe = 10$ and the indicated vision angles. The inset displays the radius of gyration as a function of effective alignment-vision ratio $\Omega_a/(\Omega_v\theta^2)$.

APPENDIX E: RADIUS OF GYRATION

In terms of its eigenvalues λ_1 and λ_2 of the radius-of-gyration tensor G_{mm} , the radius of gyration R_g is given by

$$R_g^2 = \lambda_1 + \lambda_2. \quad (E1)$$

Figure 18 presents R_g as a function of the alignment-vision ratio. For single-file motion in a nearly linear (rodlike) conformation, $R_g^2/N^2 = 1$. For single-file motion with snakelike conformations, the ratio is less than unity, and approaches $R_g^2/N^2 = 1/N$ for flexible-polymer-like conformations. The same value is obtained for compact, dislike structures.

For high ratios $\Omega_a/\Omega_v = 4$ to 25, where polar alignment dominates and elongated worm-like swarms prevail, Fig. 18 indeed shows that R_g^2/N^2 is larger compared to the regime with $\Omega_a/\Omega_v < 1$, where vision dominates and compact clusters are present. For $\Omega_a/\Omega_v \gtrsim 4$, the radius of gyration increases with decreasing vision angle. The radius of gyration starts to increase with Ω_a/Ω_v significantly earlier for lower angles because cohesion and thus cluster formation is suppressed for smaller visual signals, which favors wormlike swarms.

Similarly to the behavior of the asphericity, see Sec. B 2, we can collapse all data of the radius of gyration for $\theta \leq \pi/4$ onto a single master curve by employing an effective scaled variable $\Omega_a/(\Omega_v\theta^2)$, as demonstrated in the inset of Fig. 18. It is important to note that this rescaling is limited to vision angles $\theta \geq \pi/4$, as when the dilute phase is approached for vision angles $\theta \leq \pi/8$, vision plays an insignificant role, and, irrespective of the alignment strength $\Omega_v/\Omega_a \in [0.1, 20]$, the dilute phase or the dispersed-cluster phase always prevails.

APPENDIX F: GLOBAL POLARIZATION

In Fig. 19, the polarization order parameter P [see Eq. (14)], is depicted for a fixed maneuverability ratio of $\Omega_v/\Omega_a = 4$, and various activities Pe and vision angles θ . For $\theta \lesssim \pi/8$, the particles are randomly oriented, resulting in a dilute phase or dispersed cluster phase; compare Fig. 12.

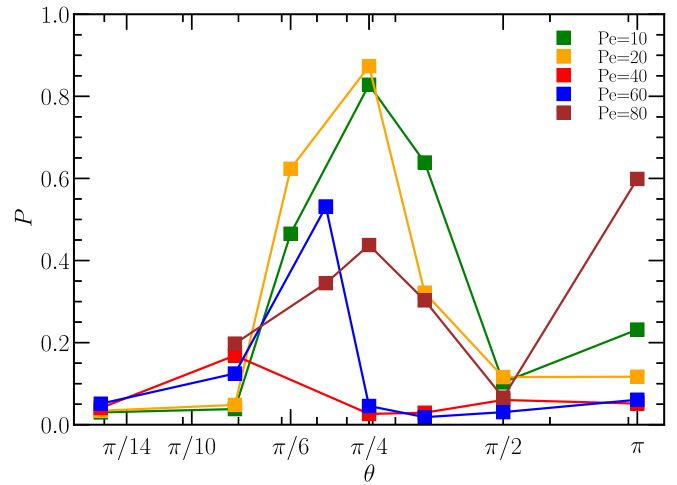


FIG. 19. Polarization order parameter P at different activities Pe , $\Omega_a/\Omega_v = 4$, $N=1250$, and vision angles θ .

Consequently, the polarization order parameter, P , nearly vanishes.

As θ increases to $\theta \gtrsim \pi/8$, for $Pe = 10$ and $Pe = 20$, the value of P grows, reaching approximately $P = 0.8$ at $\theta = \pi/4$. This indicates the formation of large wormlike swarms. However, as θ further increases to $\theta = \pi/2$, P decreases, signaling the transition to immobile compact aggregates. In the case of $Pe = 40$ and $Pe = 60$, a different behavior is observed. Initially, for small θ , P increases with θ for $\theta \lesssim \pi/6$. However, subsequently, around $\theta \approx \pi/4$, P nearly vanishes again due to the appearance of milling structures. At $Pe = 80$, a similar trend is observed, where at $\theta = \pi/2$, occasional transitions from wormlike swarming to milling occur, resulting in a low P value. However, as θ reaches π , the value of P increases again as it re-enters the wormlike swarming phase.

In summary, a high value of P is a characteristic feature of the wormlike swarming phase, while close-packed compact structures, milling, and dilute phases correspond to low values of P .

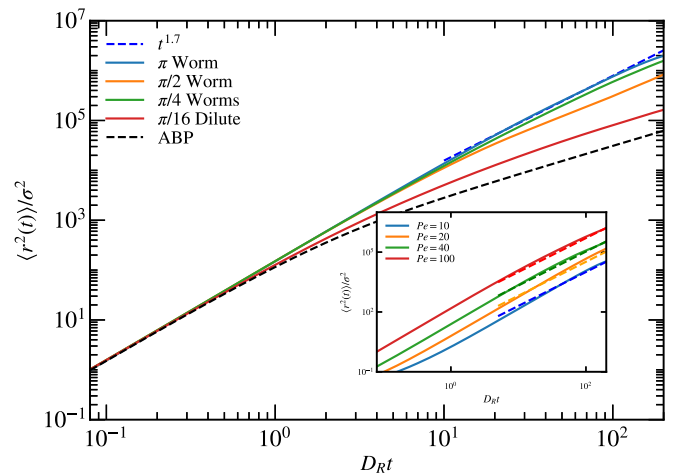


FIG. 20. Mean-square displacement for $Pe = 100$, $\Omega_a/\Omega_v = 10$, and the indicated θ . Inset: Mean-square displacement for the indicated Pe values and vision angle $\theta = \pi/4$.

TABLE II. Values of the persistence length ξ_r and ξ_p obtained for wormlike swarms for $Pe = 60$ and $\Omega_a/\Omega_v = 10$.

θ	$\pi/4$	$\pi/2$	π
ξ_p/σ	206.42	83.25	341.56
ξ_r/σ	173.22	79.31	292.56

APPENDIX G: MEAN-SQUARE DISPLACEMENT

The MSD for $Pe = 10$, $\theta = \pi/4$, and various maneuverability ratios is displayed in Fig. 9. We complement these results by the MSD data for $Pe = 100$, $\Omega_a/\Omega_v = 10$, and various vision angles θ , as shown in Fig. 20. The wormlike swarms at large vision angles $\theta \geq \pi/4$ display predominantly ballistic motion. Even for very small $\theta = \pi/16$, the motion is more persistent than the usual diffusive ABP behavior for long times. Thus, the alignment interaction strongly stabilizes the superdiffusive motion of wormlike swarms. This should be compared with the behavior of wormlike motion with only vision-based steering, where the MSD is nearly indistinguishable from that of single ABPs because the leader particle, which is not aware of its followers, dominates the dynamics of the whole aggregate. The inset in Fig. 20 illustrates the MSD values for the indicated Pe at $\theta = \pi/4$. The fitted lines correspond to $\langle \mathbf{r}^2(t) \rangle / \sigma^2 \sim (Pe D_{Rt})^{1.7}$, indicating that there is similar superdiffusive motion observed across the activities in the wormlike swarm phase. Of course, at very long times, the motion should become diffusive.

APPENDIX H: SPATIAL CORRELATION FUNCTION AND PERSISTENCE LENGTH

We characterize the spatial correlations of a wormlike swarm by the spatial angular correlation function,

$$C_e(\mathbf{r}) = \left\langle \frac{\sum_{i,j \neq i} \mathbf{e}_i \cdot \mathbf{e}_j \delta(\mathbf{r} - (\mathbf{r}_i - \mathbf{r}_j))}{\sum_{i,j \neq i} \delta(\mathbf{r} - (\mathbf{r}_i - \mathbf{r}_j))} \right\rangle, \quad (\text{H1})$$

where \mathbf{e}_i and \mathbf{e}_j are the orientation vector of particle i and j particles, respectively. This spatial correlation function can be

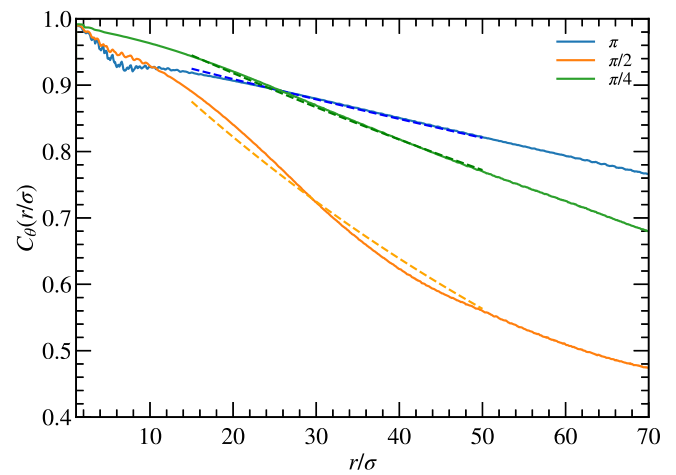


FIG. 21. Spatial angular correlation function of iABPs in the wormlike swarm phase in the $Pe = 60$ and $\Omega_a/\Omega_v = 10$. The dashed lines show exponential fits to the data.

used to extract the information about the persistence length as

$$\left\langle \sum_{i,j \neq i} \mathbf{e}_i \cdot \mathbf{e}_j \delta(\mathbf{r} - (\mathbf{r}_i - \mathbf{r}_j)) \right\rangle = B \exp(-|\mathbf{r}_i - \mathbf{r}_j|/\xi_r). \quad (\text{H2})$$

We measure the spatial persistence length ξ_r of elongated wormlike swarms, see Fig. 21, and compare it to the persistence length ξ_p obtained from autocorrelation. As expected, we find that the two measures of persistence length exhibit a remarkable similarity in the case of elongated worms; see Table II. We believe that the temporal correlation is a better approach for accurately estimating the persistence length because the thickness and the limited length of the wormlike swarms limit the accuracy of the spatial correlation function in terms of the persistence of the swarm trajectory. In contrast, the temporal correlation analysis allows us to record data for longer periods, providing a more comprehensive estimation of the persistence length.

- [1] J. Elgeti, R. G. Winkler, and G. Gompper, Physics of microswimmers—single particle motion and collective behavior: a review, *Rep. Prog. Phys.* **78**, 056601 (2015).
- [2] C. Bechinger, R. Di Leonardo, H. Löwen, C. Reichardt, G. Volpe, and G. Volpe, Active particles in complex and crowded environments, *Rev. Mod. Phys.* **88**, 045006 (2016).
- [3] S. Ramaswamy, The mechanics and statistics of active matter, *Annu. Rev. Condens. Matter Phys.* **1**, 323 (2010).
- [4] M. R. Shaebani, A. Wysocki, R. G. Winkler, G. Gompper, and H. Rieger, Computational models for active matter, *Nat. Rev. Phys.* **2**, 181 (2020).
- [5] T. Vicsek and A. Zafeiris, Collective motion, *Phys. Rep.* **517**, 71 (2012).
- [6] A. Cavagna and I. Giardina, Bird flocks as condensed matter, *Annu. Rev. Condens. Matter Phys.* **5**, 183 (2014).
- [7] D. J. Pearce, A. M. Miller, G. Rowlands, and M. S. Turner, Role of projection in the control of bird flocks, *Proc. Natl. Acad. Sci. USA* **111**, 10422 (2014).
- [8] B. L. Partridge, The structure and function of fish schools, *Sci. Am.* **246**, 114 (1982).
- [9] L. Gómez-Nava, R. Bon, and F. Peruani, Intermittent collective motion in sheep results from alternating the role of leader and follower, *Nat. Phys.* **18**, 1494 (2022).
- [10] I. Aoki, A simulation study on the schooling mechanism in fish, *Nippon Suisan Gakkaishi* **48**, 1081 (1982).
- [11] M. Ballerini, N. Cabibbo, R. Candelier, A. Cavagna, E. Cisbani, I. Giardina, V. Lecomte, A. Orlandi, G. Parisi, A. Procaccini *et al.*, Interaction ruling animal collective behavior depends on topological rather than metric distance: Evidence from a field study, *Proc. Natl. Acad. Sci. USA* **105**, 1232 (2008).

- [12] B. Dai, J. Wang, Z. Xiong, X. Zhan, W. Dai, C.-C. Li, S.-P. Feng, and J. Tang, Programmable artificial phototactic microswimmer, *Nat. Nanotechnol.* **11**, 1087 (2016).
- [13] M. Rubenstein, A. Cornejo, and R. Nagpal, Programmable self-assembly in a thousand-robot swarm, *Science* **345**, 795 (2014).
- [14] A. C. Tsang, E. Demir, Y. Ding, and O. S. Pak, Roads to smart artificial microswimmers, *Adv. Intell. Syst.* **2**, 1900137 (2020).
- [15] B. Hartl, M. Hübl, G. Kahl, and A. Zöttl, Microswimmers learning chemotaxis with genetic algorithms, *Proc. Natl. Acad. Sci. USA* **118**, e2019683118 (2021).
- [16] C. W. Reynolds, Flocks, herds and schools: A distributed behavioral model, *Computer Graphics* **21**, 25 (1987).
- [17] I. D. Couzin, J. Krause, R. James, G. D. Ruxton, and N. R. Franks, Collective memory and spatial sorting in animal groups, *J. Theor. Biol.* **218**, 1 (2002).
- [18] I. D. Couzin, J. Krause, N. R. Franks, and S. A. Levin, Effective leadership and decision-making in animal groups on the move, *Nature (London)* **433**, 513 (2005).
- [19] T. Vicsek, A. Czirók, E. Ben-Jacob, I. Cohen, and O. Shochet, Novel type of phase transition in a system of self-driven particles, *Phys. Rev. Lett.* **75**, 1226 (1995).
- [20] J. Toner and Y. Tu, Long-range order in a two-dimensional dynamical XY model: How birds fly together, *Phys. Rev. Lett.* **75**, 4326 (1995).
- [21] A. Martín-Gómez, D. Levis, A. Díaz-Guilera, and I. Pagonabarraga, Collective motion of active Brownian particles with polar alignment, *Soft Matter* **14**, 2610 (2018).
- [22] G. Grégoire and H. Chaté, Onset of collective and cohesive motion, *Phys. Rev. Lett.* **92**, 025702 (2004).
- [23] B. Szabo, G. J. Szöllösi, B. Gönci, Z. Jurányi, D. Selmeczi, and T. Vicsek, Phase transition in the collective migration of tissue cells: Experiment and model, *Phys. Rev. E* **74**, 061908 (2006).
- [24] Y. Zhao, T. Ihle, Z. Han, C. Huepe, and P. Romanczuk, Phases and homogeneous ordered states in alignment-based self-propelled particle models, *Phys. Rev. E* **104**, 044605 (2021).
- [25] H. Chaté, F. Ginelli, G. Grégoire, and F. Raynaud, Collective motion of self-propelled particles interacting without cohesion, *Phys. Rev. E* **77**, 046113 (2008).
- [26] R. Kürsten and T. Ihle, Dry active matter exhibits a self-organized cross sea phase, *Phys. Rev. Lett.* **125**, 188003 (2020).
- [27] C. B. Caporusso, P. Digregorio, D. Levis, L. F. Cugliandolo, and G. Gonnella, Motility-induced microphase and macrophase separation in a two-dimensional active Brownian particle system, *Phys. Rev. Lett.* **125**, 178004 (2020).
- [28] A. P. Solon, H. Chaté, and J. Tailleur, From phase to microphase separation in flocking models: The essential role of nonequilibrium fluctuations, *Phys. Rev. Lett.* **114**, 068101 (2015).
- [29] P. Digregorio, D. Levis, A. Suma, L. F. Cugliandolo, G. Gonnella, and I. Pagonabarraga, Full phase diagram of active Brownian disks: From melting to motility-induced phase separation, *Phys. Rev. Lett.* **121**, 098003 (2018).
- [30] A. Wysocki, R. G. Winkler, and G. Gompper, Cooperative motion of active Brownian spheres in three-dimensional dense suspensions, *Europhys. Lett.* **105**, 48004 (2014).
- [31] F. Peruani, A. Deutsch, and M. Bär, Nonequilibrium clustering of self-propelled rods, *Phys. Rev. E* **74**, 030904(R) (2006).
- [32] M. Abkenar, K. Marx, T. Auth, and G. Gompper, Collective behavior of penetrable self-propelled rods in two dimensions, *Phys. Rev. E* **88**, 062314 (2013).
- [33] M. Bär, R. Großmann, S. Heidenreich, and F. Peruani, Self-propelled rods: Insights and perspectives for active matter, *Annu. Rev. Condens. Matter Phys.* **11**, 441 (2020).
- [34] D. Strömbom, Collective motion from local attraction, *J. Theor. Biol.* **283**, 145 (2011).
- [35] L. Barberis and F. Peruani, Large-scale patterns in a minimal cognitive flocking model: Incidental leaders, nematic patterns, and aggregates, *Phys. Rev. Lett.* **117**, 248001 (2016).
- [36] R. Bastien and P. Romanczuk, A model of collective behavior based purely on vision, *Sci. Adv.* **6**, eaay0792 (2020).
- [37] R. S. Negi, R. G. Winkler, and G. Gompper, Emergent collective behavior of active Brownian particles with visual perception, *Soft Matter* **18**, 6167 (2022).
- [38] M. R. D'Orsogna, Y.-L. Chuang, A. L. Bertozzi, and L. S. Chayes, Self-propelled particles with soft-core interactions: Patterns, stability, and collapse, *Phys. Rev. Lett.* **96**, 104302 (2006).
- [39] Z. Cheng, Z. Chen, T. Vicsek, D. Chen, and H.-T. Zhang, Pattern phase transitions of self-propelled particles: Gases, crystals, liquids, and mills, *New J. Phys.* **18**, 103005 (2016).
- [40] N. H. P. Nguyen, E. Jankowski, and S. C. Glotzer, Thermal and athermal three-dimensional swarms of self-propelled particles, *Phys. Rev. E* **86**, 011136 (2012).
- [41] Y.-L. Chuang, T. Chou, and M. R. D'Orsogna, Swarming in viscous fluids: Three-dimensional patterns in swimmer- and force-induced flows, *Phys. Rev. E* **93**, 043112 (2016).
- [42] M. Durve, A. Saha, and A. Sayeed, Active particle condensation by non-reciprocal and time-delayed interactions, *Eur. Phys. J. E* **41**, 49 (2018).
- [43] X. Wang, P.-C. Chen, K. Kroy, V. Holubec, and F. Cichos, Spontaneous vortex formation by microswimmers with retarded attractions, *Nat. Commun.* **14**, 56 (2023).
- [44] B. Li, Z.-X. Wu, and J.-Y. Guan, Collective motion patterns of self-propelled agents with both velocity alignment and aggregation interactions, *Phys. Rev. E* **99**, 022609 (2019).
- [45] R. Lukeman, Y.-X. Li, and L. Edelstein-Keshet, Inferring individual rules from collective behavior, *Proc. Natl. Acad. Sci. USA* **107**, 12576 (2010).
- [46] F. Ginelli and H. Chaté, Relevance of metric-free interactions in flocking phenomena, *Phys. Rev. Lett.* **105**, 168103 (2010).
- [47] A. Peshkov, S. Ngo, E. Bertin, H. Chaté, and F. Ginelli, Continuous theory of active matter systems with metric-free interactions, *Phys. Rev. Lett.* **109**, 098101 (2012).
- [48] A. Kolpas, M. Busch, H. Li, I. D. Couzin, L. Petzold, and J. Moehlis, How the spatial position of individuals affects their influence on swarms: A numerical comparison of two popular swarm dynamics models, *PLoS ONE* **8**, e58525 (2013).
- [49] P. Rahmani, F. Peruani, and P. Romanczuk, Topological flocking models in spatially heterogeneous environments, *Commun. Phys.* **4**, 206 (2021).
- [50] O. Chepizhko, D. Saintillan, and F. Peruani, Revisiting the emergence of order in active matter, *Soft Matter* **17**, 3113 (2021).
- [51] T. Bäuerle, R. C. Löffler, and C. Bechinger, Formation of stable and responsive collective states in suspensions of active colloids, *Nat. Commun.* **11**, 1 (2020).
- [52] T. Bäuerle, A. Fischer, T. Speck, and C. Bechinger, Self-organization of active particles by quorum sensing rules, *Nat. Commun.* **9**, 3232 (2018).

- [53] F. A. Lavergne, H. Wendehenne, T. Bäuerle, and C. Bechinger, Group formation and cohesion of active particles with visual perception dependent motility, *Science* **364**, 70 (2019).
- [54] S. Das, G. Gompper, and R. G. Winkler, Confined active Brownian particles: Theoretical description of propulsion-induced accumulation, *New J. Phys.* **20**, 015001 (2018).
- [55] S. Goh, R. G. Winkler, and G. Gompper, Noisy pursuit and pattern formation of self-steering active particles, *New J. Phys.* **24**, 093039 (2022).
- [56] N. Grønbech-Jensen and O. Farago, A simple and effective Verlet-type algorithm for simulating Langevin dynamics, *Mol. Phys.* **111**, 983 (2013).
- [57] S. Mandal, B. Liebchen, and H. Löwen, Motility-induced temperature difference in coexisting phases, *Phys. Rev. Lett.* **123**, 228001 (2019).
- [58] See Supplemental Material at <http://link.aps.org/supplemental/10.1103/PhysRevResearch.6.013118> for simulation movies.
- [59] S. P. Singh, D. A. Fedosov, A. Chatterji, R. G. Winkler, and G. Gompper, Conformational and dynamical properties of ultra-soft colloids in semi-dilute solutions under shear flow, *J. Phys.: Condens. Matter* **24**, 464103 (2012).
- [60] R. E. Isele-Holder, J. Elgeti, and G. Gompper, Self-propelled worm-like filaments: Spontaneous spiral formation, structure, and dynamics, *Soft Matter* **11**, 7181 (2015).
- [61] A. Attanasi, A. Cavagna, L. Del Castello, I. Giardina, S. Melillo, L. Parisi, O. Pohl, B. Rossaro, E. Shen, E. Silvestri, and M. Viale, Finite-size scaling as a way to probe near-criticality in natural swarms, *Phys. Rev. Lett.* **113**, 238102 (2014).
- [62] K. Tunstrøm, Y. Katz, C. C. Ioannou, C. Huepe, and I. D. C. Matthew J. Lutz, Collective states, multistability and transitional behavior in schooling fish, *PLoS Comput. Biol.* **9**, e1002915 (2013).
- [63] T. C. Schneirla, A unique case of circular milling in ants, considered in relation to trail following and the general problem of orientation, *Am. Mus. Novit.* **1253**, 1 (1944).
- [64] J. Delcourt, N. W. Bode, and M. Denoël, Collective vortex behaviors: Diversity, proximate, and ultimate causes of circular animal group movements, *Q. Rev. Biol.* **91**, 1 (2016).
- [65] N. R. Franks, A. Worley, K. A. Grant, A. R. Gorman, V. Vizard, H. Plackett, C. Doran, M. L. Gamble, M. C. Stumpe, and A. B. Sendova-Franks, Social behaviour and collective motion in plant-animal worms, *Proc. R. Soc. B.* **283**, 20152946 (2016).
- [66] A. B. Sendova-Franks, N. R. Franks, and A. Worley, Plant-animal worms round themselves up in circular mills on the beach, *R. Soc. Open Sci.* **5**, 180665 (2018).
- [67] W.-J. Rappel, A. Nicol, A. Sarkissian, H. Levine, and W. F. Loomis, Self-organized vortex state in two-dimensional dictyostelium dynamics, *Phys. Rev. Lett.* **83**, 1247 (1999).
- [68] A. M. Reynolds, G. E. McIvor, A. Thornton, P. Yang, and N. T. Ouellette, Stochastic modelling of bird flocks: Accounting for the cohesiveness of collective motion, *J. R. Soc. Interface* **19**, 20210745 (2022).
- [69] Antipattern, Fungus gnat larvae travelling in procession, <https://www.youtube.com/watch?v=6MwYvLaJ6Ho>, accessed Nov. 4, 2014.
- [70] South China Morning Post, Thousands of ducks released to protect Thai rice fields from pests, <https://www.youtube.com/watch?v=6MwYvLaJ6Ho>, accessed Sept. 15, 2020.